Oxide-supported metal clusters: models for heterogeneous catalysts



2003 J. Phys.: Condens. Matter 15 R31

(http://iopscience.iop.org/0953-8984/15/2/202)

INSTITUTE OF PHYSICS PUBLISHING JOURNAL OF PHYSICS: CONDENSED MATTER

J. Phys.: Condens. Matter **14** (2002) R31–R62 PII: S0953-8984(02)30501-0

**TOPICAL REVIEW**

# Oxide-supported metal clusters: models for heterogeneous catalysts

**A K Santra and D W Goodman**[1]

Department of Chemistry, Texas A & M University, PO Box 30012, College Station, TX 77842-3012, USA

E-mail: goodman@mail.chem.tamu.edu

Received 18 September 2002
Published 20 December 2002
Online at stacks.iop.org/JPhysCM/14/R31

**Abstract**

Understanding the size-dependent electronic, structural and chemical properties of metal clusters on oxide supports is an important aspect of heterogeneous catalysis. Recently model oxide-supported metal catalysts have been prepared by vapour deposition of catalytically relevant metals onto ultra-thin oxide films grown on a refractory metal substrate. Reactivity and spectroscopic/microscopic studies have shown that these ultra-thin oxide films are excellent models for the corresponding bulk oxides, yet are sufficiently electrically conductive for use with various modern surface probes including scanning tunnelling microscopy (STM). Measurements on metal clusters have revealed a metal to nonmetal transition as well as changes in the crystal and electronic structures (including lattice parameters, band width, band splitting and core-level binding energy shifts) as a function of cluster size. Size-dependent catalytic reactivity studies have been carried out for several important reactions, and time-dependent catalytic deactivation has been shown to arise from sintering of metal particles under elevated gas pressures and/or reactor temperatures. *In situ* STM methodologies have been developed to follow the growth and sintering kinetics on a cluster-by-cluster basis. Although several critical issues have been addressed by several groups worldwide, much more remains to be done. This article highlights some of these accomplishments and summarizes the challenges that lie ahead.

(Some figures in this article are in colour only in the electronic version)

[1] Author to whom any correspondence should be addressed.

  

## Contents



## 1. Introduction

Understanding the electronic structure of metal clusters supported on solid substrates is fundamental to heterogeneous catalysis [1–18] and microelectronics [19, 20]. Accordingly the size-dependent electronic structure, morphology, thermal stability, metal support interaction and chemical reactivity of metal clusters have been studied extensively [1–44]. These studies have shown that the energy and peak width for the core-levels and valence bands of metal clusters varies with cluster size. These changes have been interpreted in terms of initial- and/or final-state effects arising from differences in the charge density and core–hole screening of bulk metal atoms and atoms within small metal clusters. Reducing the size of a metal cluster to a diameter (near the nm regime) comparable to the de Broglie wavelength ($\lambda = h/p$, where $h =$ Planck′s constant and $p =$ momentum) of an electron can dramatically change the physical properties of the cluster. These changes have been referred to as 'quantum size effects' since the properties of these 'nano-particles' can be best described using quantum mechanics. Thus for small clusters the metallic properties are attenuated and the electronic structure of the small cluster approaches that of an isolated atom. X-ray photoelectron spectroscopy (XPS), ultraviolet photoelectron spectroscopy (UPS), metastable impact electron spectroscopy (MIES), work function measurements, Auger electron spectroscopy (AES), temperature-programmed desorption (TPD) and scanning tunnelling microscopy/spectroscopy (STM/STS) have been used to follow this size-dependent electronic structure. STM–STS data have shown [16] that a metal–nonmetal transition occurs with a decrease in cluster size. STM has been particularly useful in studying the changes in catalytic reactivity of these supported model systems with respect to cluster morphology, temperature and pressure [45–73].

In the bulk form, Au is chemically inert relative to other Pt group metals, e.g., corrosion and oxidation resistance, high ductility and malleability, and a very high electronegativity

(comparable with selenium). With respect to electronegativity, gold is known to exist in a stable formal oxidation state of −1 in CsAu. Recently Haruta and co-workers [74–80] have shown that Au clusters, deposited as finely dispersed, small clusters (<5 nm diameter) on reducible metal oxides like $TiO_2$, $Fe_2O_3$ and $Co_3O_4$, exhibit catalytic activity for a wide array of industrially important reactions; i.e., CO oxidation at sub-ambient temperatures (<200 K), preferential oxidation of CO in the presence of excess hydrogen, hydrogenation, $NO_x$ reduction, partial oxidation of hydrocarbons and selective oxidation of higher alkenes. This unusual catalytic activity has been shown to depend markedly on the Au cluster size.

In general, bulk metal oxides of typical catalytic supports are wide bandgap materials and therefore present formidable charging problems making them unsuitable candidates for electron spectroscopic and STM measurements. However, these difficulties have been circumvented in our laboratories by synthesizing well ordered, ultra-thin oxide films on refractory metal substrates [81–98]. These films are thin enough (<5 nm) to prevent charging, yet thick enough to exhibit electronic and chemical properties comparable to the corresponding bulk oxide.

In this review recent work, where metal clusters have been synthesized on thin film oxide supports, is highlighted. In particular, the effect of Pd cluster size on acetylene cyclotrimerization and the CO + NO reaction, as well as Au cluster size on CO oxidation, is discussed. The ultimate goal of these studies is to establish a definitive correlation among cluster size, cluster electronic properties and cluster chemical/catalytic properties.

## 2. Experimental details

$TiO_2$(110) single crystals (Princeton Scientific) become sufficiently conductive for STM and electron spectroscopic measurements after cycles of $Ar^+$ sputtering and annealing to 700–1000 K, and, therefore, have been used directly as supports for model catalyst preparation. A typical $TiO_2$(110) surface obtained after such a preparation procedure is shown in figure 1(a) (50 nm × 50 nm). An atomically resolved (6 nm × 6 nm) image of the same surface is shown in figure 1(b). After calibration of the scanner using a graphite (HOPG) sample, the distances between adjacent atoms along the [001] and [1$\bar{1}$0] directions were measured to be 0.3 and 0.65 nm, respectively, in excellent agreement with the unit cell of the (1 × 1) $TiO_2$(110) surface [58, 64]. We have also been able to prepare high quality, well ordered $TiO_2$(110) ultra-thin films on a Mo(110) substrate [98]. For nonreducible and wide bandgap oxides like $SiO_2$, MgO and $Al_2O_3$, the preparation of well ordered, ultra-thin films on refractory metals is crucial to these studies, particularly for electron spectroscopy and STM. Since optimizing conditions for such preparations is demanding, these procedures will be discussed in detail separately. Metal depositions were typically carried out by resistive evaporation of a high purity metal wire wrapped around a W filament in ultrahigh vacuum. By controlling the filament current, the doser-to-substrate distance and the substrate temperature, fine control can be achieved with respect to cluster size and density. Four different UHV chambers equipped with XPS, AES, high resolution electron energy loss spectroscopy (HREELS), low energy electron diffraction (LEED), STM (RHK Tech. and Omicron) and ion-scattering spectroscopy (ISS) were used for these studies [10, 58, 70, 74].

## 3. Preparation and characterization of ultra-thin ordered films

### *3.1. $Al_2O_3$*

Bulk alumina is a wide bandgap (8.7 eV) material; therefore, to enhance the conductivity we have prepared ultra-thin ordered $Al_2O_3$ 0.5–3 nm thick on Re(0001), Ta(110) and Mo(110) by

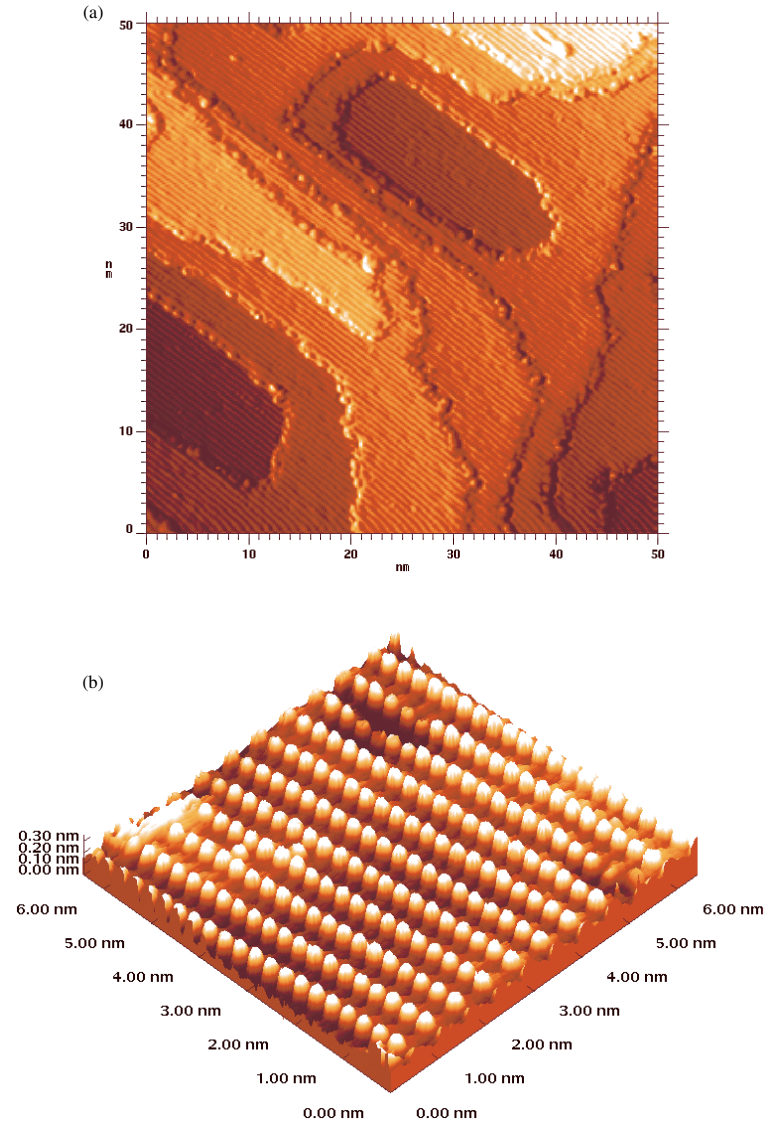


**Figure 1.** STM image of a typical $TiO_2(110)$ sample after reduction and thorough cleaning procedure at (a) 50 nm × 50 nm and (b) atomic resolution (6 nm × 6 nm).

vapour depositing Al at 300 K and $1 \times 10^{-5}$ mbar $O_2$ pressure [95–99]. Generally the film grows two dimensionally initially then three dimensionally at higher coverages. A typical STM picture of the of the film at an early growth stage (0.35 MLE) on Re(0001) is shown in figure 2(a) indicating laterally uniform two-dimensional island growth. As the film continues to grow in a layer-by-layer fashion, the exposed Re surface is covered relatively quickly (figure 2(b)). The two-dimensional growth is also in agreement with previous studies of Madey and co-workers [99] using LEIS. The best quality flat films were obtained at coverages near 2 MLE. In figure 2(c), an STM image of a 2.2 MLE film is shown showing flat, ordered growth. However, STM data show that the films become more irregular at higher coverages although LEED data indicate long range order.

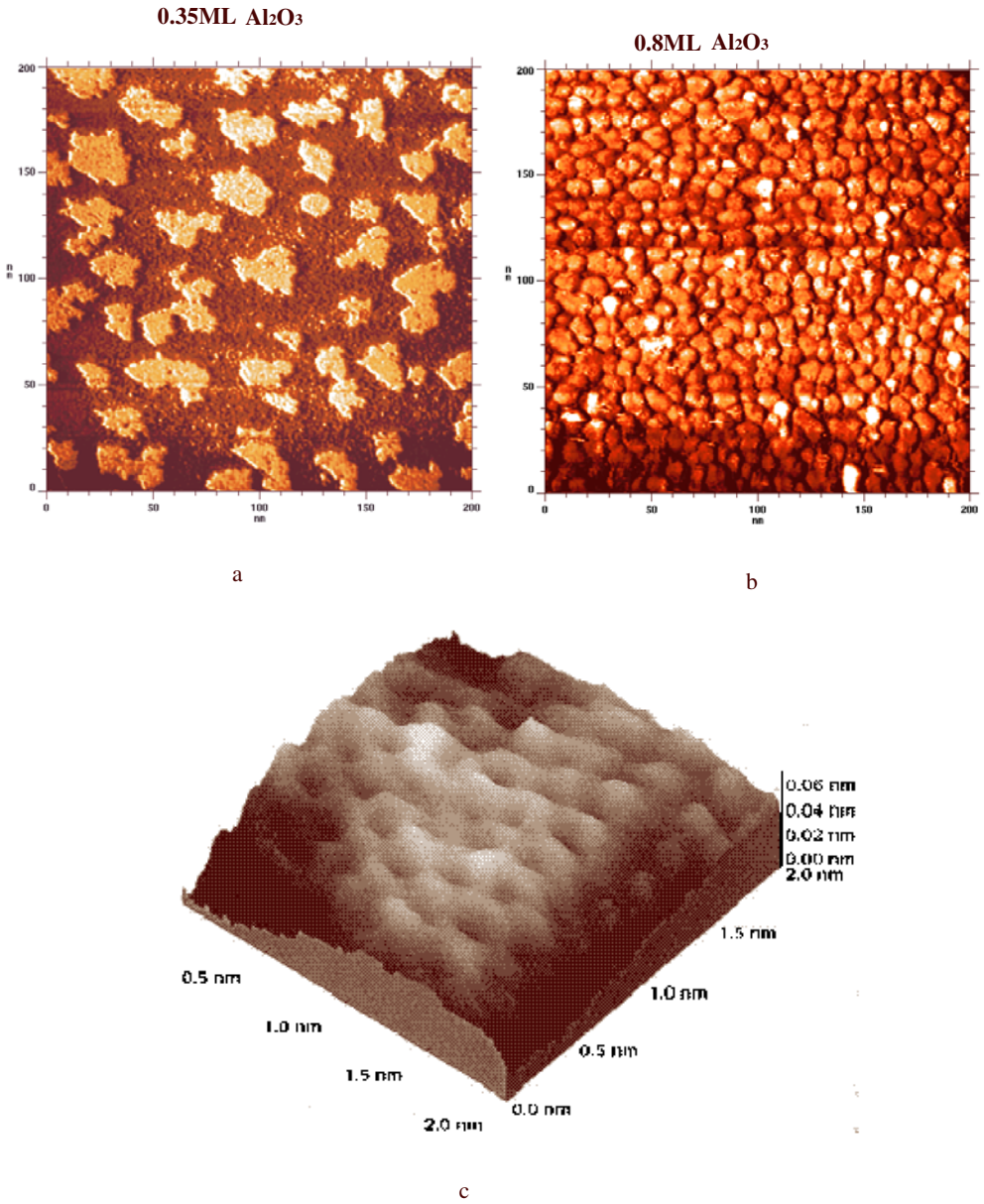


**Figure 2.** STM images of $Al_2O_3$ film grown on Re(0001) at (a) 0.35 MLE (200 nm × 200 nm) and (b) 0.8 MLE (200 nm × 200 nm). (c) Three-dimensional image (2 nm × 2 nm) view from a 2.2 MLE film.

An AES spectrum of a 2.0 nm film has a prominent $Al^{3+}$ (LVV) feature at ∼45 eV and an O (KLL) feature at ∼500 eV. The absence of a peak at 68 eV, characteristic of $Al^0$, indicates that the film is fully oxidized. Features attributable to the Mo(110) substrate can be seen in the 100–250 eV region. The thicknesses of the oxide films were estimated from the attenuation of the AES intensity ratio of the $Al^{3+}$ (LVV) feature relative to the Mo(MNN) feature. XPS analysis (O 1s, Al2s and Al 2p) confirmed that the $Al_2O_3$ films grow stoichiometrically.

Stoichiometric $Al_2O_3$ films are also consistent with high resolution electron energy loss (HREELS) data [96]. The fundamental modes of the surface optical phonons are located below 1000 $cm^{-1}$. The thick films are characterized by three fundamental modes at 370, 640 and 875 $cm^{-1}$, while the thin films are characterized by two fundamental modes at 590 and 860 $cm^{-1}$. The energies of the three modes for the thick films agree well with previously reported vibrational data for $Al_2O_3$ [100–103] while the data for a 0.44 nm film are consistent with those reported by Frederick *et al* for $Al_2O_3$ [104, 105].

There are two additional methods for preparing ultra-thin, well ordered $Al_2O_3$ films:

(i) oxidizing single crystals of Al [106, 107] and
(ii) oxidizing AlNi [108, 109] or $Ni_3Al$ [110–112] single crystals.

Method (ii) has received considerable attention because of the superior quality of films obtained with this method.

### *3.2. $SiO_2$*

Extremely high quality ultra-thin, flat and ordered $SiO_2$ films have been grown by sequential deposition of 0.5 MLE of Si at 300 K followed by oxidation at 800 K in $1 \times 10^{-7}$ mbar of $O_2$ (5 min). This process was repeated several times depending upon the desired film thickness. Finally the film was annealed at 1100–1200 K in $1 \times 10^{-7}$ mbar $O_2$ for 30 min. The thickness of the $SiO_2$ films was estimated from the relative attenuation of the Mo substrate AES intensity [88, 93]. Typically the optimum deposition rates were found to be near 12 min/MLE. These films (>0.8 nm thick) were very stable up to 1200–1300 K (since no loss of either Si or oxygen was detected with AES). The stoichiometry of the films was confirmed by the absence of Si- or SiO-related features in AES and XPS [90].

As reported by Freund and co-workers [113] and in a recent report from our laboratory [94], the films prepared by sequential deposition indeed grow flat and epitaxial. In figure 3, STM images of the $SiO_2$ films at 0.8 nm are shown. The inset at the top right of this figure shows an STS acquired for a film of ∼0.8 nm thickness showing a bandgap greater than 8 eV (bulk $SiO_2$ has a bandgap of 8.9 eV). The corresponding LEED pattern acquired for this film is presented in the inset at the top left, and shows a sharp hexagonal pattern indicative of long range order. This STM image indeed reveals that the film is extremely flat and well ordered [114]. A 'bulklike' bandgap and a sharp hexagonal LEED pattern not only indicate that the film is extremely suitable for model studies but also prove that these films are structurally and electronically similar to bulk $SiO_2$. Very recently, single-crystalline $SiO_2$ films have also been prepared on Ni(111) [115]. Oxidation of Si(111) to $SiO_2$ has also been attempted by a number of groups [116–118].

### *3.3. MgO*

Several efforts to prepare well ordered MgO films have been made using single crystals of Ag [119, 121], Fe [122] and Mo [82–86, 120]. SPA-LEED analysis of the films grown on the first two substrates showed the growth mode to be of mosaic type. However, very high quality well ordered MgO(100) films were prepared on Mo(100) by co-depositing Mg (12 min/MLE) and oxygen ($1 \times 10^{-6}$ mbar) at 600 K followed by annealing in vacuum at 1100 K. Using this method extremely sharp ($1 \times 1$) LEED patterns were obtained on films >15 MLE. However, due to insufficient tunnelling, STM imaging of these films was not possible. Unlike $SiO_2$ or $Al_2O_3$, as discussed earlier in the text, these films initially grow as islands. However, appropriate annealing of >15 MLE thick films (prepared at 600 K) led to crystalline films

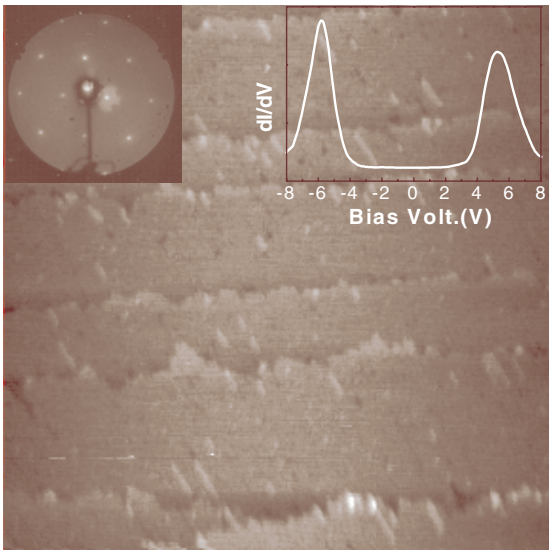


**Figure 3.** STM image (400 nm × 400 nm) of a typical $SiO_2$ (0.8 nm) film on Mo(112). The top right-hand inset shows the STS while that on the left-hand side shows a sharp hexagonal LEED pattern taken from the same surface.

with a sharp (1 × 1) LEED pattern. UPS investigations from our laboratory revealed that such films are 'bulklike' and have a bandgap structure very close to the bulk material; AES and XPS reveal that these films are stoichiometric. The bulklike chemical nature of these films was also confirmed using water and NO as probe molecules. In line with the results on single-crystal MgO(100), formation of $N_2O$ via a $(NO)_2$ intermediate has also been detected on these high quality MgO films using IRAS and has been interpreted to arise from the presence of large, flat terraces with a low concentration of point defects [87].

## 4. Electronic structure and morphology

### *4.1. Electron spectroscopy*

Electron spectroscopies, particularly photoemission (XPS and UPS), have been extensively used to study the electronic structure of small metal clusters deposited on well characterized model supports [7, 21–44]. XPS has been used to monitor the changes in the core-level binding energy with respect to the bulk metal ($\Delta E_c = E_c(\text{cluster}) - E_c(\text{bulk})$). UPS has been used to investigate the valence band region as well as changes in the work function of the system as a function of cluster size. The core-level binding energy generally decreases and the splitting or width of the valence band increases with an increase in cluster size, ultimately reaching the bulk value. The difference between the core-level binding energy of the bulk metal and the smallest clusters ($\Delta E_c$) has been observed to vary from substrate to substrate mainly depending upon the conducting nature of the support. These general trends have often been noted; however, their origins remain controversial. The simplest expression for the core-level binding energy is $E_c = E_{final}$ (after photoemission) $- E_{initial}$ (before photoemission) and therefore is largely determined by the differences in the electronic charge densities of the initial and final states of the system. Final state effects, or changes in $E_{final}$, can arise due to differences in the screening of the core hole created after photoemission. For a solid, it is convenient to separate

the total screening into contributions from intra-atomic and extra-atomic screening. Intra-atomic screening mainly depends on the element; however, extra-atomic screening depends on the surrounding environment, i.e. co-ordination number, ligand attached and substrate. For example, for a cluster, due to its finite dimensions, changes in the extra-atomic screening become very important; a reduction in the extra-atomic screening compared to that in the bulk metal can lead to an increase in the core-level binding energy. Initial state contributions are due to differences in charge density before photoemission and may arise from a variety of factors such as

(i) changes in the electronic structure of the clusters with respect to the bulk metal;
(ii) changes in chemical environment at the interface;
(iii) surface core-level shift and
(iv) defect-induced metal–substrate interactions.

Figures 4(a) and (b) show changes in the Au $4f_{7/2}$ core level as a function of Au coverage (measure of cluster size) on $TiO_2(110)$ and $SiO_2$/Mo(110) [56]. A similar plot on amorphous graphite is shown in figure 5. In general, the Au $4f_{7/2}$ binding energy with respect to the bulk metal (84.0 eV) decreases with an increase in cluster size, finally converging to the bulk value at large cluster sizes. It should be noted that the largest shifts ($\Delta E_c$) observed on three different substrates are 0.55, 0.8 and 1.6 eV for graphite, $TiO_2(110)$ and $SiO_2$, respectively. Such differences have been explained as due to the relative abilities of these substrates to screen the core hole after photoemission, i.e., a final-state contribution. Graphite, the most conductive among the three, screens best and produces the least shift in the core-level binding energy. In general there is an increase in the FWHM of the core-level XP spectra with a decrease in the average cluster size, which probably relates to the unavoidable distribution of cluster sizes.

Figure 5 shows how the Au 5d splitting, Au $4f_{7/2}$ binding energy and Au $E_F$ change with a change in cluster size on an amorphous graphite substrate. Wertheim and co-workers [21–29] have explained such changes as due to the poor conductivity of the substrate leading to an unscreened positive charge after photoemission. However, an increase in the Au $E_F$ could also be due to a metal–nonmetal transition as the cluster size decreases; this possibility will be discussed further in the next section. A decrease in the Au 5d splitting with a decrease in cluster size could be due to a decrease in the coordination number as shown by Mason and co-workers [30–35], taking the Au–Cd alloy system as an example. Dicenzo and co-workers [44] have shown how the binding energy of the Au $4f_{7/2}$ level changes with the mean co-ordination number of small clusters (figure 6). If one assumes that the unscreened charge considered by Wertheim and co-workers [21–29] is the only factor responsible for the changes in binding energy, then the dashed line of figure 6 follows. The dashed line considers only the effect of the coulombic term, $e^2/2R$, where $R$ is the radius of the cluster [44]. Deviation of the experimental points from the expected dashed line clearly indicates that effects other than coulombic ones contribute.

Ultraviolet photoemission (valence band) spectra with increasing Pd coverage on $Al_2O_3$/Re(0001) substrate have been measured [36] and are shown in figure 7. A gradual evolution of metallic valence bands with increasing cluster size is a manifestation of the increasing density of states near the Fermi level and the appearance of dispersing bands parallel and perpendicular to the substrate. The latter has been attributed to the formation of crystallites with a preferred orientation. The appearance of dispersion may also be used to define the boundary between a metallic and nonmetallic state of the clusters. In the data presented, this transition appears to take place at an average cluster size of $\sim$2.5 nm.

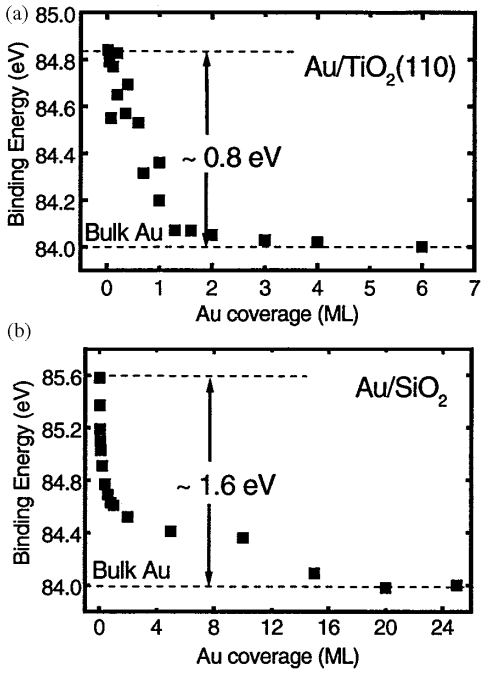


**Figure 4.** Plots of the Au $4f_{7/2}$ core-level binding energy as a function of Au cluster coverage (ranging from 0.02 MLE to bulk) on $TiO_2(110)$ (a) and $SiO_2$ (b) surfaces.

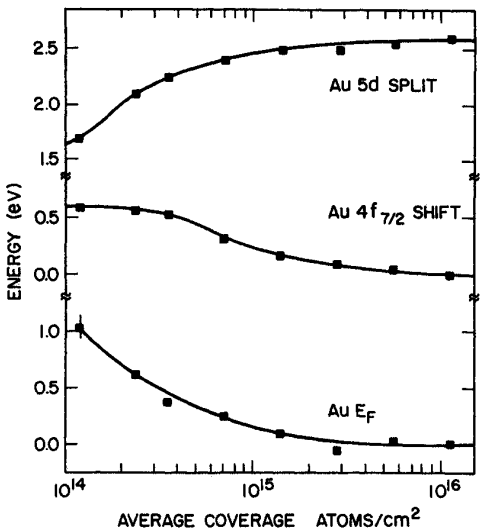


**Figure 5.** Coverage dependence plots of the Au 4f binding energy, the position of the Au Fermi edge and Au 5d splitting (from [21]).

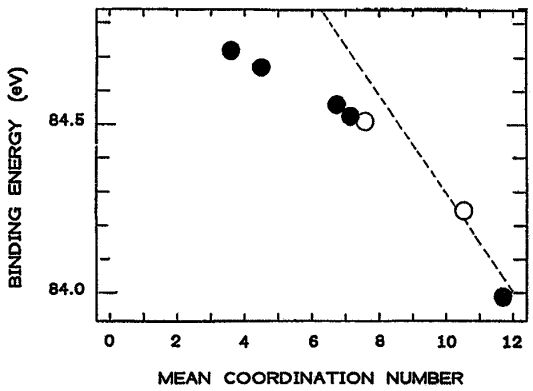


**Figure 6.** Au $4f_{7/2}$ binding energy versus coordination number plotted for mass-selected $Au_n$ clusters deposited on amorphous carbon. The open circles are data for the clusters obtained by vapour deposition on amorphous carbon; the average co-ordination numbers for these were determined by correlating their corresponding Au 5d splitting with those obtained for mass-selected clusters. The dashed line shows the binding energies expected for supported Au clusters allowing only for the Coulomb energy of the positively charged clusters in the photoemission (from [44]).

### *4.2. Scanning tunnelling microscopy*

The growth and morphology of metal clusters has been studied extensively with STM; however, tunnelling characteristics sufficient for imaging have limited these studies to oxides with

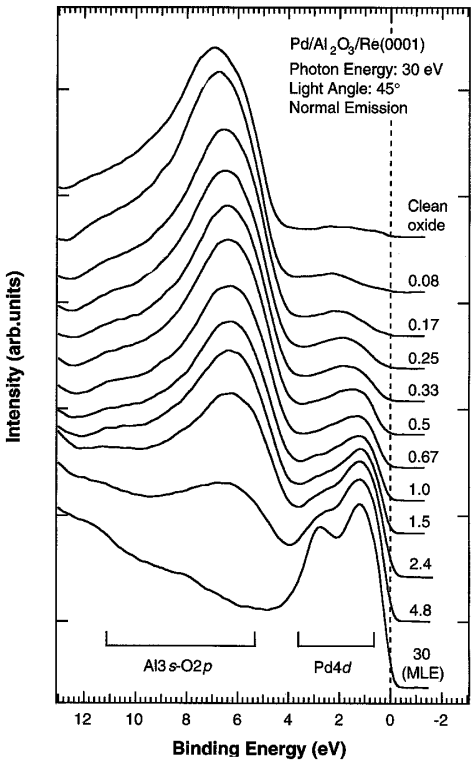


**Figure 7.** Normal emission spectra of the valence bands taken at 30 eV photon energy showing an overview of the growth of the Pd clusters for coverages ranging from 0.08 to 30 MLE. The binding energy refers to the Fermi edge of the Re(0001) substrate, which is identical to that of the thick metallic Pd film at a coverage of 30 MLE.

relatively low bandgaps (<2–3 eV). Catalytically important wide bandgap supports such as MgO, $SiO_2$ or $Al_2O_3$ in their bulk forms are not suitable for STM studies; $TiO_2$, for which the reduced form is suitably conductive, has been thoroughly studied. In our laboratory, to circumvent the tunnelling difficulties of bulk insulators, well ordered flat ultra-thin oxide films have been prepared on refractory metal substrates as described earlier in this article. These ultra-thin films are not only conductive enough for STM measurements but have been shown to have the structural and chemical properties of their bulk counterparts.

*4.2.1. Cluster growth as a function of metal coverage.* Several simple models for the growth morphologies have been proposed for metal clusters deposited on various substrates. These models generally assume that the substrate contains randomly distributed nucleation sites and that the metal cluster size depends on the distribution of these fixed nucleation sites and the amount of metal deposited. For amorphous carbon substrates the number of nucleation sites is large. Egelhoff and Tibbetts [41] proposed that on substrates with an abundance of nucleation sites deposition initially yields isolated adatoms. These isolated adatoms, in turn, diffuse randomly on the substrate, eventually coalescing with another adatom or adatom clusters. Since the nucleation sites are randomly distributed and the diffusion itself is a random phenomenon, the result is a distribution of cluster sizes at each metal coverage.

The growth of Au clusters on $TiO_2(110)$ has been investigated in detail by STM and STS. The constant current STM micrographs in figure 8 show [12] how the size/shape and number

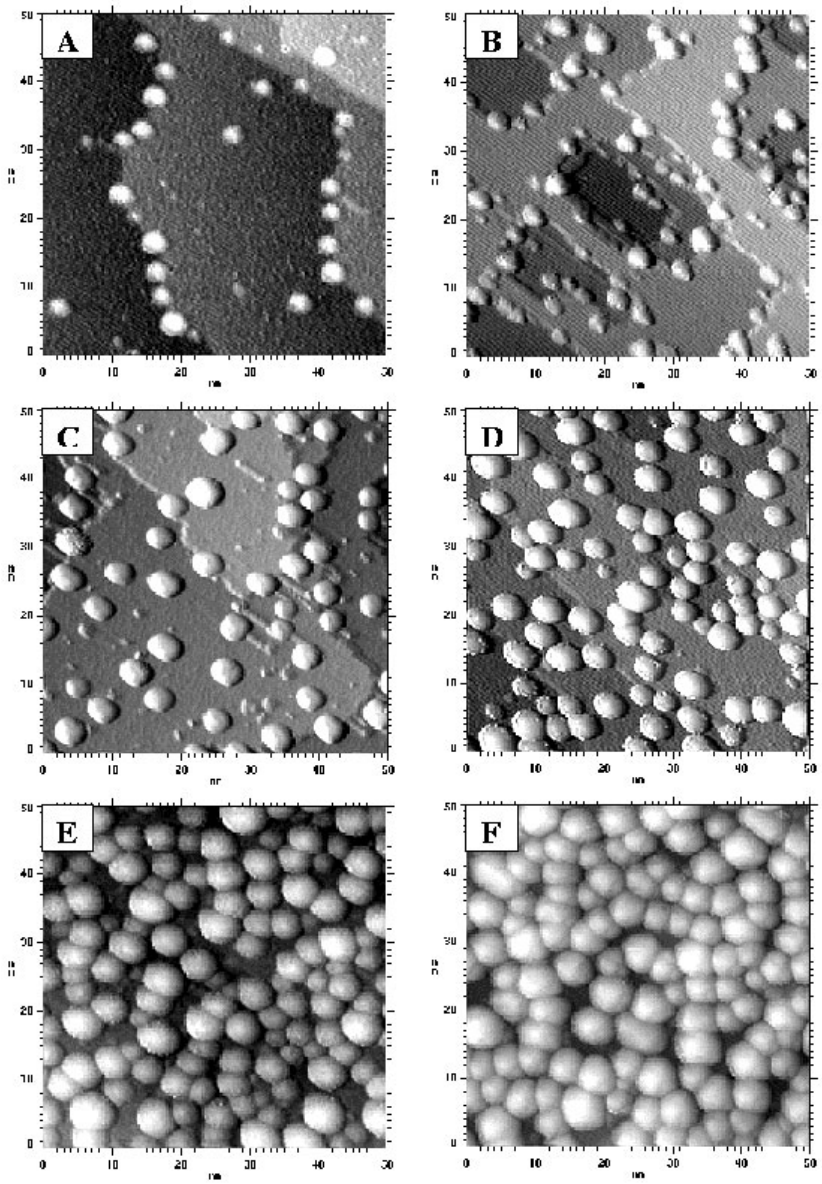


**Figure 8.** A set of 50 nm × 50 nm STM images (2.0 V, 1.0 nA) of $TiO_2$(110)-(1 × 1) with different Au coverages: (A) 0.10 MLE, (B) 0.25 MLE, (C) 0.50 MLE, (D) 1.0 MLE, (E) 2.0 MLE and (F) 4.0 MLE. With increasing coverage, Au clusters grow and gradually cover the surface.

density of the clusters change with respect to the quantity of Au deposited. At relatively low coverages (0.1 MLE) of Au, hemispherical three-dimensional clusters with diameters of 2–3 nm and heights of 1–1.5 nm are observed to decorate preferentially along the step edges. Well dispersed quasi-two-dimensional clusters, having a height of 0.3–0.6 nm and a diameter of 0.5–1.5 nm, can be seen on the large terraces. With increasing Au coverage, the clusters grow larger with little increase in cluster density. However, even at 4.0 MLE, some portions of the $TiO_2$ substrate are still visible. The average diameter and number

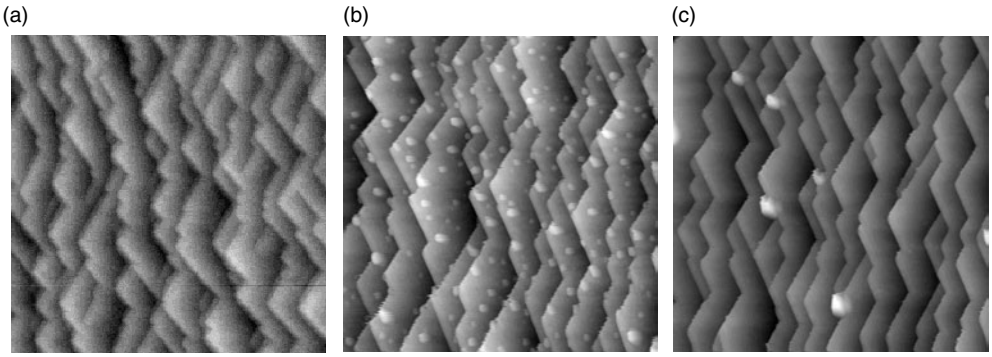


**Figure 9.** STM image of (a) p(1 × 3)-O reconstructed Mo(112) surface (200 nm × 200nm), (b) 1.6 MLE Ag deposited on the same surface at room temperature (200 nm × 200 nm) and (c) after annealing the surface at 750 K for 2 min (200 nm × 200 nm).

density of the clusters increase simultaneously with an increase in metal coverage until at a certain stage (as long as there is sufficient room on the surface to separate them) metal size increases at the expense of the number density. In other words, the number density of the clusters goes through a maximum [123]. Our results for Ag on $Al_2O_3$/Re(0001) [124] and Pd on $TiO_2$(110) [64] have also shown a similar trend of cluster growth at room temperature. Several other extremely high quality STM micrographs have also been reported by Besenbacher and co-workers addressing the morphology and adhesion energy of Cu and Pd clusters on $Al_2O_3$/NiAl(110) substrates [125–128].

*4.2.2. Growth morphology versus metal–support interaction.* As discussed in the previous section, for flat, well ordered surfaces, in particular, the number of nucleation sites is relatively small, therefore the cluster size distribution is expected to be a function of the diffusion barrier depending critically on the metal–support interaction. Therefore, a surface with a relatively large metal–support interaction typically is expected to yield smaller clusters with high number densities while large clusters with low number densities are expected on surfaces with a relatively weak metal–support interaction. Since the metal adatom diffusion barrier is critically dependent on the surface temperature, increasing the surface temperature should enhance the rate of cluster sintering.

In order to investigate the relative differences in the growth mode of Ag metal we have prepared a p(1 × 3)-O reconstructed surface as well as epitaxial $MoO_2$ films [129]. A typical p(1 × 3)-O reconstructed surface (consisting of well ordered terraces and steps) is shown in the large area (200 nm × 200 nm) STM image of figure 9(a). Deposition of 1.6 MLE of Ag at room temperature yielded relatively large (∼5.5 nm) three-dimensional clusters (figure 9(b)) with a lower number density than that observed for Co on Mo(110) [130]. Annealing this surface at 750 K for 2 min led to sintering (figure 9(c)) and movement of the clusters to the step edges.

In a second set of experiments, a surface with adjacent $MoO_2$ and Mo(112) domains was prepared by vacuum annealing a p(1 × 2)-O reconstructed surface at 1400 K. The large area (300 nm × 300 nm) STM micrograph of figure 10(a) shows the simultaneous existence of two distinctly different types of surface region. The magnified STM image (100 nm × 100 nm) of figure 10(b) shows that the domains of the type labelled as '1' consist of islands of thin layer $MoO_2$ on a Mo(112) surface and the domains of the type labelled as '2' consist essentially of

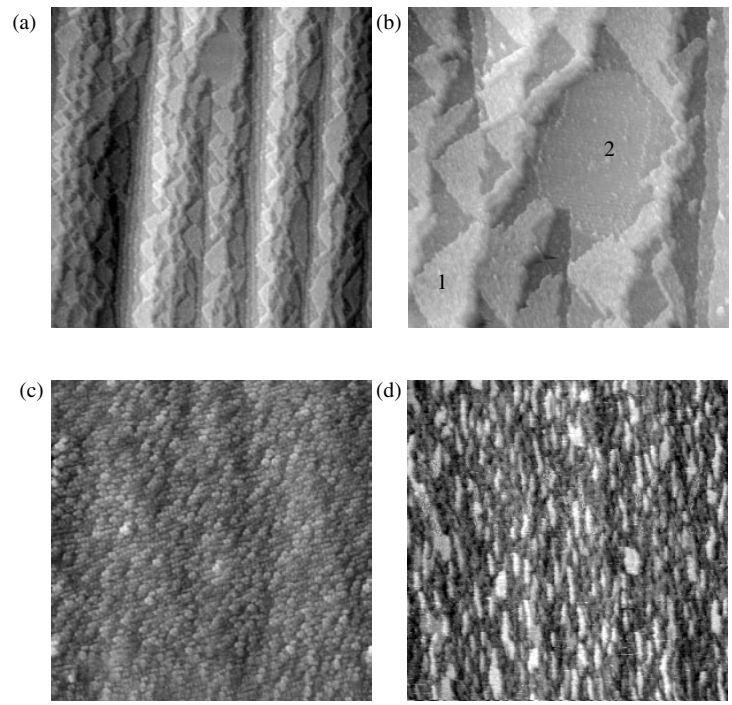


**Figure 10.** STM image of (a) a surface (300 nm × 300 nm) with adjacent $MoO_2$ and bare Mo(112) nano-domains, (b) zoomed in image (100 nm × 100 nm) of the same surface, (c) surface with 1.6 MLE of Ag deposited at room temperature (200 nm × 200 nm) and (d) after annealing the surface (200 nm × 200 nm) at 750 K for 10 min.

clean Mo(112). The STM of figure 10(c), acquired after deposition of 1.6 MLE of Ag at room temperature onto the surface of figure 10(a), shows that Ag clusters grow very uniformly, with smaller size (∼3 nm) and with a higher number density relative to that of figure 9(b). This not only indicates that the surface has a higher average metal–support interaction compared to the oxygen pre-adsorbed surface (figure 9(b)) but also suggests that the two different regions (1 and 2) behave similarly with respect to the nucleation and growth of Ag clusters at this stage. A similar growth mode on the two regions could be due to the following factors:

(a) similar metal–support interaction strengths and/or
(b) sufficiently large metal–support interactions at room temperature that the clusters undergo very little surface diffusion.

To check for the relative contribution of (b), the surface temperature was increased by increments in order to increase the rate of cluster surface diffusion. In figure 10(d), an STM image (200 nm × 200 nm) is shown after annealing the surface at 750 K for 10 min. The image shows that the metal clusters have diffused and sintered to form two-dimensional Ag nanostructures with elongated shapes. More interestingly, the two-dimensional Ag nanostructures are preferentially located on the bare metal sites. Therefore, it is quite clear from these results that the bare metal areas have a significantly greater metal–support interaction, yet can be differentiated with respect to their sintering behaviour at higher temperatures.

A surface with $MoO_2$ layers with varying thicknesses was prepared by vacuum annealing a p(1 × 3)-O reconstructed surface of the type shown in figure 9(a) at 1400 K. The large area STM

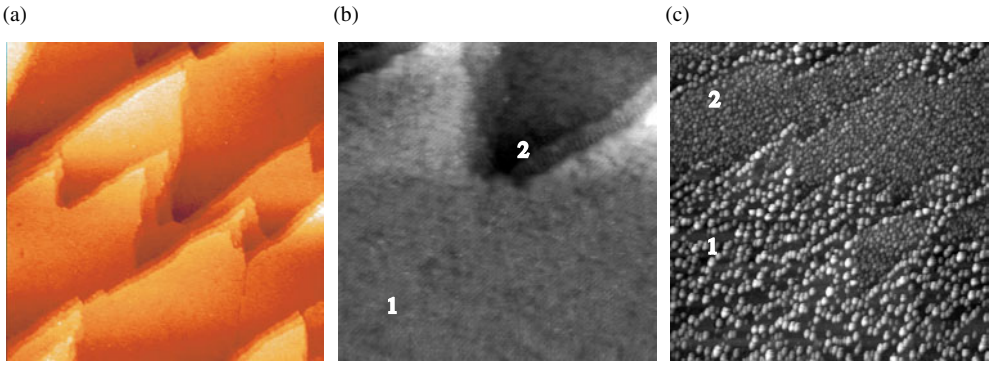


**Figure 11.** STM image of (a) a surface (200 nm × 200 nm) with layers of $MoO_2$ at different thickness, (b) zoomed in image (50 nm × 50 nm) of the same surface and (c) after 1.6 MLE Ag deposited at room temperature (200 nm × 200 nm).

image (200 nm × 200 nm) of figure 11(a) shows that the surface consists of $MoO_2$ layers of varying thicknesses. The high resolution STM image of figure 11(b) shows the ordered growth of $MoO_2$ and the variation in the thickness of the oxide films. An STM image following the deposition of 1.6 MLE Ag at room temperature is shown in figure 11(c). The STM image shows two distinctly different regions with variations in the cluster-size distribution due to the variation of the strength of the metal–support interaction. As expected, on the thicker oxide domains the average cluster size is larger (∼4.5 nm) with a lower number density, while on the relative thin oxide domains the cluster size is relatively small (∼3 nm) with a relatively high number density. This is consistent with the results of figure 10(c) that show that, at room temperature, the cluster size and shape on bare Mo(112) and domains of a thin oxide layer of $MoO_2$ are indistinguishable. As anticipated, the thinner oxide layers, because of geometrical strain due to lattice mismatch with the substrate, have a higher surface free energy compared with the thicker layers and thus interact more strongly with adsorbed metal clusters.

Very recently, Bowker and co-workers [131–135] have proposed a strong metal–support interaction for the $Pd/TiO_2(110)$ system including reverse spill-over of $TiO_x$ onto Pd particles after annealing at higher temperatures.

*4.2.3. Sintering of metal clusters.* An increase in the average size of metal clusters has been observed either with an increase in substrate temperature or an increase in ambient pressure. Sintering has been used as a key reason for deactivation of supported catalysts in many industrially important reactions. However, the details of sintering and regeneration of catalysts are still unclear. There are two generally accepted pathways to sintering: (i) atom migration (also known as Ostwald ripening), and (ii) entire cluster migration. Figure 12 shows typical STM images of Ag particles on a $SiO_2/Mo(112)$ substrate after deposition at room temperature and annealing at 700 K in UHV [72]. It is apparent from these two images that there is an overall increase in the average cluster size with a decrease in the number density as a result of annealing. Figure 13 shows STM images of Ag clusters on $TiO_2$ as deposited and subsequent to exposure to an elevated pressure of reactant gas [60]. A detailed quantitative analysis of the average cluster size revealed a transformation from mono- to bi modal distribution with respect to increase in the ambient gas pressure and therefore has been understood as due to the Ostwald ripening. However, from these experiments it is not possible

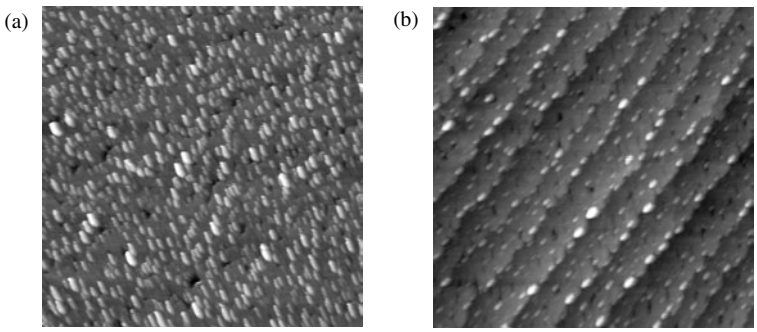


**Figure 12.** An STM image of Ag (3 MLE) deposited on $SiO_2$ (1.5 MLE): (a) as deposited at 300 K and (b) as-deposited clusters after annealing at 700 K for 2 min under UHV.

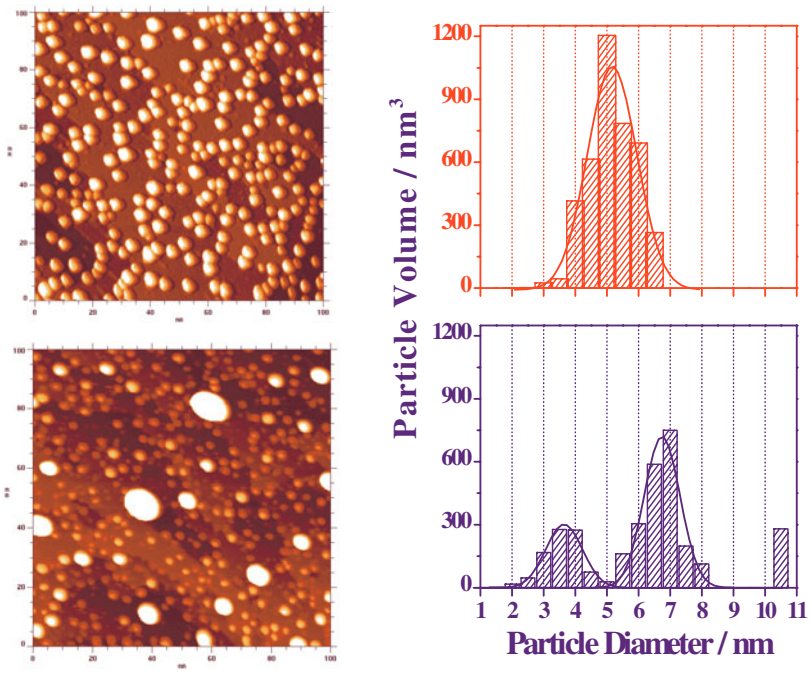


**Figure 13.** STM images (100 nm × 100 nm) of 2 MLE Ag/$TiO_2$(110) (a) before and (b) after exposure to 10 mbar $O_2$ for 120 min at 298 K. Corresponding size distributions of the particles are shown in the bar plots. A bimodal distribution results after the $O_2$ treatment.

to comment on the relative contribution from the cluster migration route. A similar behaviour has also been noticed for Au/$TiO_2$ [60] and Pd/$TiO_2$ [64] systems.

### *4.3. In situ scanning tunnelling microscopy*

In the previous section an overview was presented showing the general growth behaviour of metal clusters on oxide supports. However, the inherent difficulty of imaging the same cluster(s) throughout the experimental procedure remains an important challenge. Only recently has this been carried out by the novel use of an *in situ* STM tip-shadowing technique.

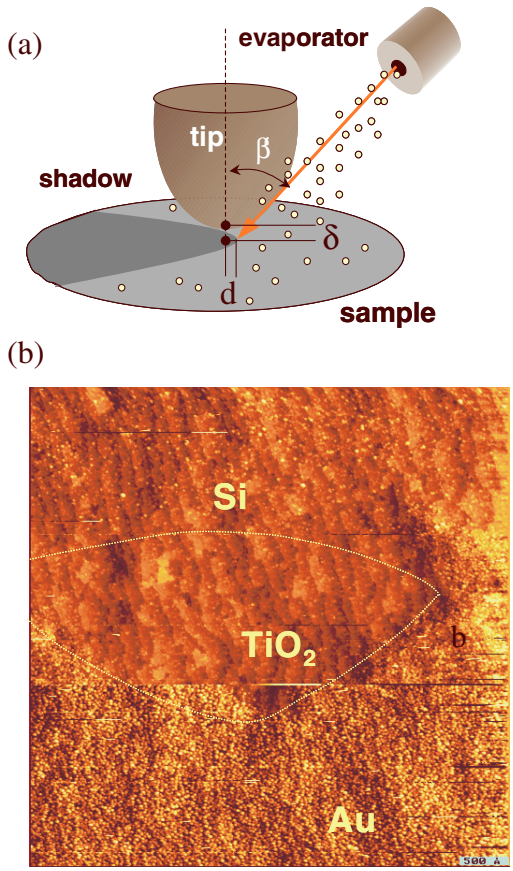


**Figure 14.** (a) A schematic model for the tip and metal doser position while carrying out tip-shadow experiments and (b) an STM image showing overlapping shadows from Si and Au dosers, respectively (from [123]).

Using this methodology, the behaviour of an identical set of clusters has been monitored with varying experimental conditions such as

(i) changes in ambient pressure and exposure time,
(ii) changes in substrate temperature,
(iii) change in cluster size with an increase in metal coverage and
(iv) growth of dissimilar metal clusters in the presence of clusters from a second metal.

The typical setup of the shadowing technique methodology is described in detail elsewhere [123]. In brief, metal dosing is carried out while the STM tip is in the tunnelling position using a specially designed metal doser. This method creates a shadow of the tip on the substrate as shown in figure 14. Using the tip shadow as a 'marker' it is possible to locate the same set of clusters at various times during the experimental procedure. Growth of Au clusters on a $TiO_2(110)$ substrate has been monitored on a cluster-by-cluster basis using this technique. Generally the cluster size and the number density of the clusters increase with the increase in Au coverage. Importantly, the clusters grow quickly at the onset of deposition and reach ∼90% of their saturation value at 0.2 MLE coverage [123].

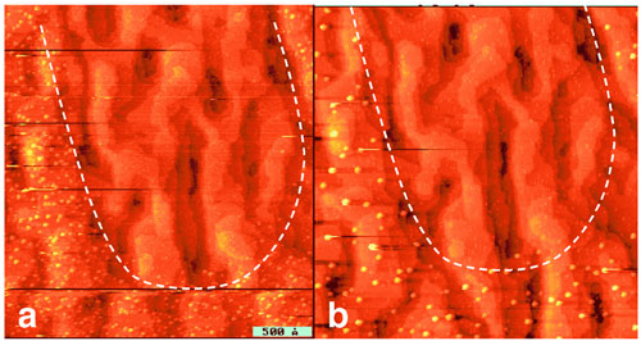


**Figure 15.** STM images of Au/$TiO_2$(110) around the tip shadow after and before annealing to 950 K (from [123]).

Using this technique it also possible to follow the thermal sintering process on a cluster-by-cluster basis and distinguish between Ostwald ripening (atom diffusion) and cluster diffusion. However, due to the thermal drift of the STM tip, such experiments are extremely difficult and efforts to perfect the approach are currently in progress. Figures 15(a) and (b) show STM images of a Au/$TiO_2$(110) surface at room temperature and after a 30 min anneal at 950 K. It is noteworthy that apart from a general increase in the size of the clusters, there is clear evidence for some of the smaller clusters diffusing up to 5 nm [123]. Similar observations have been made recently by Egdell and co-workers [136] for the Au/$TiO_2$(110) system. However, only an Ostwald ripening mechanism is apparent for Pd/$TiO_2$(110) [137]. Very recently, with *in situ* AFM, thermal diffusion and sintering phenomena of metal clusters have been studied on MgO(100) single crystals by Yang and Perry [138]. Their results for Cu/MgO(100) suggest a general increase in Cu islands with increasing surface temperature accompanied by decay, diffusion and coalescences of the islands. These results are in excellent agreement with those obtained on our model catalysts using ultra-thin oxide films.

It is relatively easy to perform *in situ* experiments by changing the ambient pressure. A study of Au/$TiO_2$(110) under elevated oxygen pressure (4 mbar) showed that Au clusters smaller than ∼4 nm are very unstable to sintering at 450 K. Oxygen at elevated pressures possibly weakens the Au–$TiO_2$ (metal–support) interaction leading to facile sintering [70]. Figure 16 shows Au clusters subjected to elevated pressures (up to 665 Pa) of CO and $O_2$ at 450 K [69]. Analysis shows that the size distribution of Au clusters changes to bimodal, peaking at ∼1 and 4 nm, respectively. A majority of the larger clusters increases by ∼25% in volume while the smaller clusters decrease in size or vanish.

More recently the growth and morphology of bimetallic clusters has been examined. For example, the growth of Au clusters in the presence of Ag clusters has been studied [123, 139]. These experiments were carried out to understand the effect of the initial metal clusters on the growth mode of the second metal, including the formation of a binary alloy. Figure 17 shows how Au nucleates and grows in the presence of Ag clusters. These *in situ* STM results show the following:

(i) initially the addition of Au leads to the growth of the existing Ag clusters with no new clusters being formed, and

(ii) once the bimetallic Au–Ag particles reach a certain size, their growth rate decreases and the nucleation/growth of new Au particles begins.

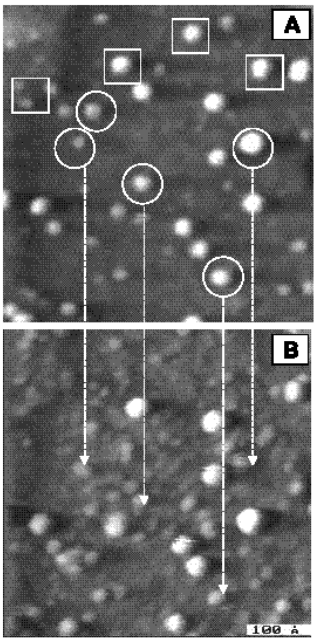


**Figure 16.** STM image of the same area taken at 450 K: (a) under UHV conditions and (b) during 665 Pa CO + $O_2$ mixture exposure. The clusters removed due to tip effects are marked by squares. The circles indicate those clusters exhibiting gradual reduction in size (from [69]).

Even though the resulting particles consist of Au and Ag (as evidenced from the increase in size of the Ag particles after Au deposition), it cannot be confirmed that alloying occurs. Further studies in combination with other techniques are necessary to understand the details of this unusual behaviour.

### *4.4. Scanning tunnelling spectroscopy*

To understand how the electronic structure of metal clusters changes with a change in cluster size, STS investigations have been carried out on Au clusters deposited on a $TiO_2(110)$ substrate. A constant current STM micrograph of 0.25 ML Au deposited onto single-crystal $TiO_2(110)$-$(1 \times 1)$ is shown in figure 18(a) [12, 16]. The deposition was carried out at 300 K followed by annealing to 850 K for 2 min. In the STM image (figure 18(a)) the Ti cations are visible; however, the $O^{2-}$ anions are not. The inter-atomic distance between the [001] rows is ∼0.65 nm. Three-dimensional Au clusters, imaged as bright protrusions, have average diameters of ∼2.6 nm and heights of ∼0.7 nm (corresponding to two to three atoms thick) and are preferentially nucleated at the step edges. Quasi-two-dimensional clusters are characterized by heights of one to two atomic layers.

Figure 18(b) shows STS data acquired for various clusters where the tunnelling current ($I$) as a function of bias voltage ($V$) is measured. The extent of the plateau at zero tunnelling current is a measure of the bandgap (along the bias voltage axis). The electronic character of these clusters is expected to vary between that of a metal and a nonmetal depending on their size. With an increase in size, clusters gradually adopt the metallic character with an enhanced density of states at the Fermi level, consistent with the UPS data of figure 7. Note that the cluster 2.5 nm × 0.7 nm in size has a larger bandgap than a 5.0 nm × 2.5 nm cluster. Smaller clusters have a nonmetallic character resulting in a significant bandgap and a reduced density of states near the Fermi level. A similar metal–nonmetal transition with respect to cluster size has also been observed for Fe clusters deposited on GaAs(110) [140]. That the very small

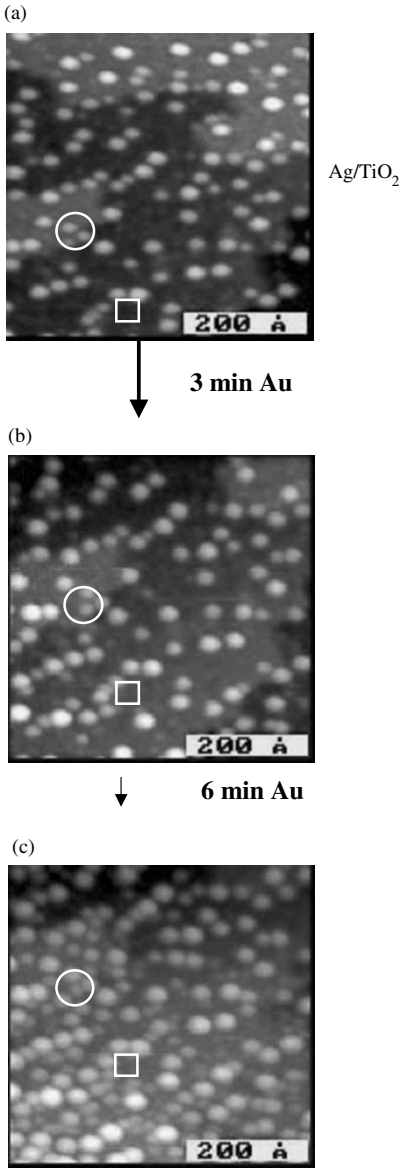


**Figure 17.** *In situ* STM images taken using the tip-shadowing technique as a function of Au deposition time, starting with an Ag deposited $TiO_2$(110) surface. Square and circle symbols are to guide the eyes to identical spots. Nucleation and growth of new Au clusters are very evident from the images.

clusters are nonmetallic could be responsible for the observed changes in the electronic and chemical properties, discussed in the following sections.

### *4.5. Transmission electron microscopy*

Transmission electron microscopy (TEM) is one of the oldest and most popular techniques for the characterization of catalysts [141]; however, TEM has limited resolution (∼0.2 nm) and

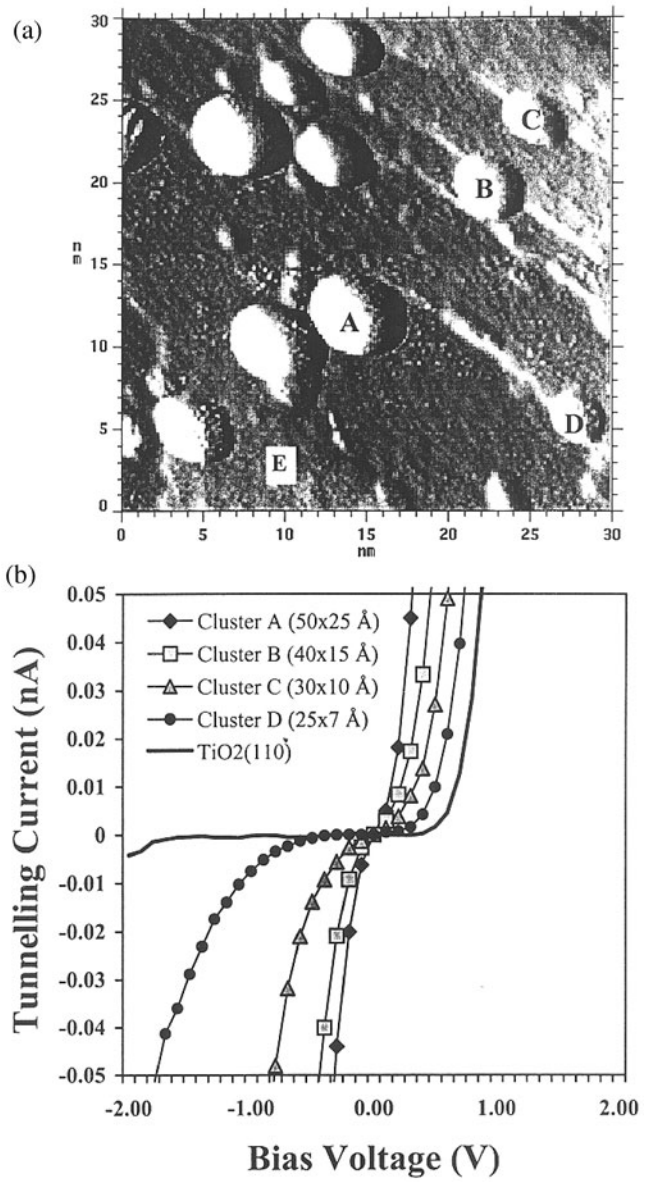


**Figure 18.** (a) A constant current STM image of 0.25 MLE Au deposited onto $TiO_2$(110)-(1 × 1) prepared just prior to a CO:$O_2$ reaction. The sample had been annealed to 850 K for 2 min. (b) STS data acquired for Au clusters of varying sizes on $TiO_2$(110)-(1 × 1). An STS of the $TiO_2$ substrate, having a wider bandgap than the Au cluster, is also shown as a point of reference.

is limited with respect to reactant environments. Poppa and co-workers [142, 143] carried out measurements on Ag/(mica or molybdenite) and Pd/MgO systems under *in situ* conditions. Recently, informative *in situ* TEM measurements have been reported by Goyhenex and Henry [144] on the Pd/MgO(100) system. An impressive TEM image of 20 MLE Pd deposited on a UHV-cleaved single crystal of MgO(100) is shown in figure 19. The average particle size is ∼60 nm with various thermodynamically stable cluster shapes displayed. Careful Pd-coverage-

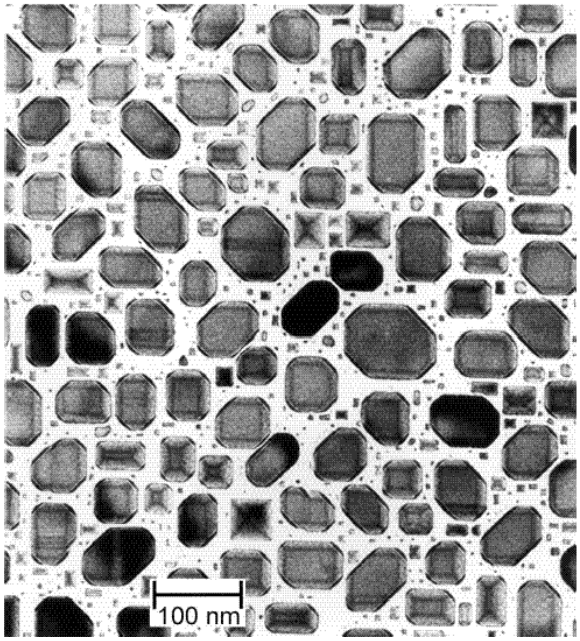


**Figure 19.** TEM image of Pd crystallites on MgO(100) (from [1]).

dependent studies using surface electron energy-loss fine structure spectroscopy (SEELFS) above the Pd $N_{23}$ edge have shown that the average lattice parameter of the deposited clusters increases with a decrease in cluster size. Freund and co-workers [145, 146] have recently carried out TEM investigations on Pt and Ta clusters on an $Al_2O_3$/NiAl(110) substrate and have correlated the average lattice parameter with cluster size. In the case of Pt particles a contraction of ∼10% in lattice parameter is noted when the particle size is reduced from 3 to 1 nm while only ∼4.5% contraction has been observed for Ta. This change in lattice parameter with particle size has been attributed to several factors: (i) surface stress, (ii) pseudomorphism and (iii) a change in the average atomic co-ordination number. In any case, a significant role of the lattice parameter is expected on the electronic and chemical properties of metal particles compared with their bulk analogue.

### *4.6. Temperature-programmed desorption and microcalorimetry*

To understand the diffusion of atoms/particles on a substrate, it is very important to obtain information about the interaction between the substrate and the metal atoms/clusters. TPD has been used to measure sublimation energies for several metal/oxide systems. Figures 20(a)–(c) show families of TPD spectra for Cu/$Al_2O_3$ [54], Au/$SiO_2$ [56] and Au/$TiO_2$ [66] systems. For the first two cases (figures 20(a) and (b)), the leading edge of the data are observed to increase continuously with metal coverage. The width of the TPD curve is a measure of the distribution of cluster diameters and heights. That is, an increase in the width of the desorption curve with an increase in metal coverage is evidence for an increase in the cluster size distribution. The lower desorption temperature peak maximum at low coverage arises because the substrate–metal interaction is less than the metal–metal interaction in the bulk metal. This also confirms that the thermally induced sintering is a much slower process compared to desorption. The heat of sublimation, $E_{sub}$, is shown in the inset as a function of metal coverage (cluster size). For

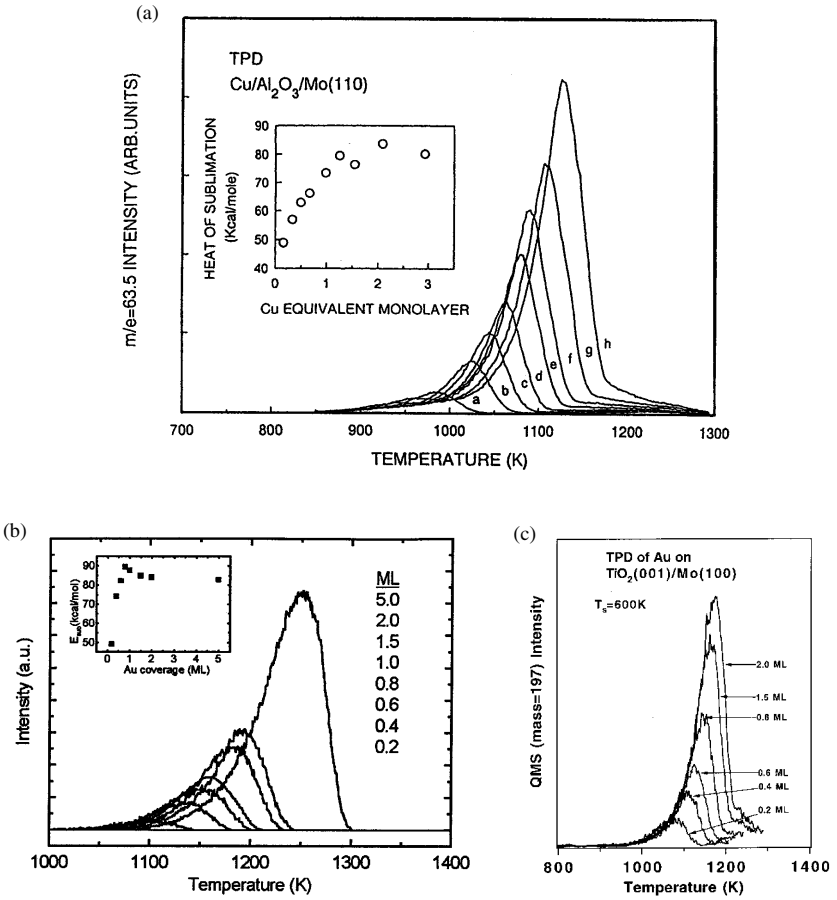


**Figure 20.** A family of TPD spectra of (a) Cu deposited on $Al_2O_3$/Mo(110), (b) Au deposited on $SiO_2$/Mo(100) and (c) Au deposited on $TiO_2$/Mo(100) at various coverages. The insets show a plot of $E_{sub}$ determined from the leading edge analysis.

higher coverages the heat of sublimation reaches the value of the bulk metal suggesting that the metal–metal interaction is dominant at the large cluster limit. The average sublimation energy for the larger Cu clusters [$Cu/Al_2O_3$/Mo(110)] is ∼323–349 kJ mol$^{-1}$, essentially the same as the bulk value, while for the smallest clusters this value is estimated to be ∼205 kJ mol$^{-1}$ [54]. For $Au/SiO_2$/Mo(110) the smallest clusters show an $E_{sub}$ of 168 kJ mol$^{-1}$ compared to a bulk value of 378 kJ mol$^{-1}$ [56]. In contrast to the behaviour observed for $Au/SiO_2$ system, $Au/TiO_2$ (figure 20(c)) shows a single desorption peak independent of the metal coverage. The leading edge analysis yields a Au substrate binding energy of 210 kJ mol$^{-1}$, a value much smaller than that observed on $SiO_2$. The dramatic difference in the sublimation energy and its invariance with the metal coverage is likely due to the fact that Au evaporates preferentially from the periphery of the clusters (weakly bound at the interface due to the interaction with the substrate) and is a precursor to Au desorption. One disadvantage of measuring the adsorption energy using TPD is that the method yields a value for the sublimation energy at the desorption temperature (a relatively high surface temperature). Extracting information relevant to the lower surface temperature (reaction temperature) is not straightforward.

A more direct technique, microcalorimetry, been used recently by Campbell and co-workers [147–150] for Pb, Ag and Cu clusters on MgO(100) and the Au/$TiO_2$(110) system. This approach yields differential heats of adsorption of the metal with varying surface temperature. This group has been able to extract heats of adsorption as a function of cluster diameter as well. Using this technique in combination with LEIS the sintering of Au particles on $TiO_2$(110) has been observed to begin at ∼400 K, yet requires >900 K for completion.

## 5. Size-dependent chemical reactivity

### *5.1. Acetylene cyclotrimerization on Pd/$Al_2O_3$ and $Pd_n$/MgO*

The cyclotrimerization of acetylene to benzene on low index single-crystal Pd surfaces has been studied extensively due to the structure sensitivity of this reaction [149–158]. For example, the Pd(111) facet is very active, yielding ten times as much benzene as seen for Pd(100); the benzene yield is essentially zero for Pd(110) [159]. This unusual structure sensitivity has prompted researchers to look for particle size effects in high surface area catalysts and on supported Pd clusters of various sizes prepared on model $Al_2O_3$/Mo(110) thin films [63]. Figure 21(a) shows TPD corresponding to benzene desorption ($m/e = 78$) as a function of Pd cluster size. These TPD data are similar to results from analogous low index single-crystal data that show distinct cluster size effects. For the smallest clusters (∼1.5–2.0 nm, cf 0.5 MLE), benzene desorption occurs predominantly above 500 K, with very little low temperature benzene evolution. With an increase in the cluster size, the high temperature peak becomes smaller while the desorption feature at 230 K increases in intensity. Both the high and low temperature benzene desorption features have been observed for benzene on the Pd(111) surface, consistent with the reaction being desorption rate limiting. Benzene desorption near 370 K has not been observed on single crystals and has been attributed to defect sites. Taking into account the benzene-coverage-dependent TPD results from single crystals, the absence of a lower temperature desorption feature (230 K) for the smaller clusters has been explained as due to their enhanced curvatures and the absence of large ⟨111⟩ terraces. The high curvature and absence of ⟨111⟩ structures preclude the formation of an ordered, compressed overlayer of weakly bound benzene in the tilted configuration and favour the more strongly bound benzene, bonded parallel to the surface.

The idea of a 'template' effect on a hexagonal Pd(111) face requiring seven contiguous Pd atoms in a flat geometry for the production of a strongly bound benzene has been tested using mass-selected Pd clusters deposited on MgO thin film. This work suggests a minimum requirement of a seven-atom cluster for the synthesis of a strongly bound flat-lying benzene desorbing at higher temperature ($T_d \sim 430$ K). However, to relate this observation to a 'template' effect one has to assume that flat, seven-atom clusters form on the MgO surface in a hexagonal geometry. Figure 21(b) shows TPD data for benzene from Pd/MgO surfaces with varying cluster size ($Pd_n$, $1 \leqslant n \leqslant 30$) [160]. In each case, the total coverage of Pd is constant at 0.28%. It is noteworthy that these authors have observed the production of benzene even for a single Pd atom, though producing only weakly adsorbed ($T_d \sim 300$ K) benzene in the tilted configuration. Density functional calculations also show that a single Pd atom can be active for benzene production when bonded to an oxygen vacancy of the MgO substrate.

### *5.2. NO and CO reactions on Pd and Cu/$Al_2O_3$*

There has been considerable interest in identifying alternatives to expensive Pt/Rh catalysts used for three-way automobile exhaust gas conversion [161–164]. CO and NO reaction studies

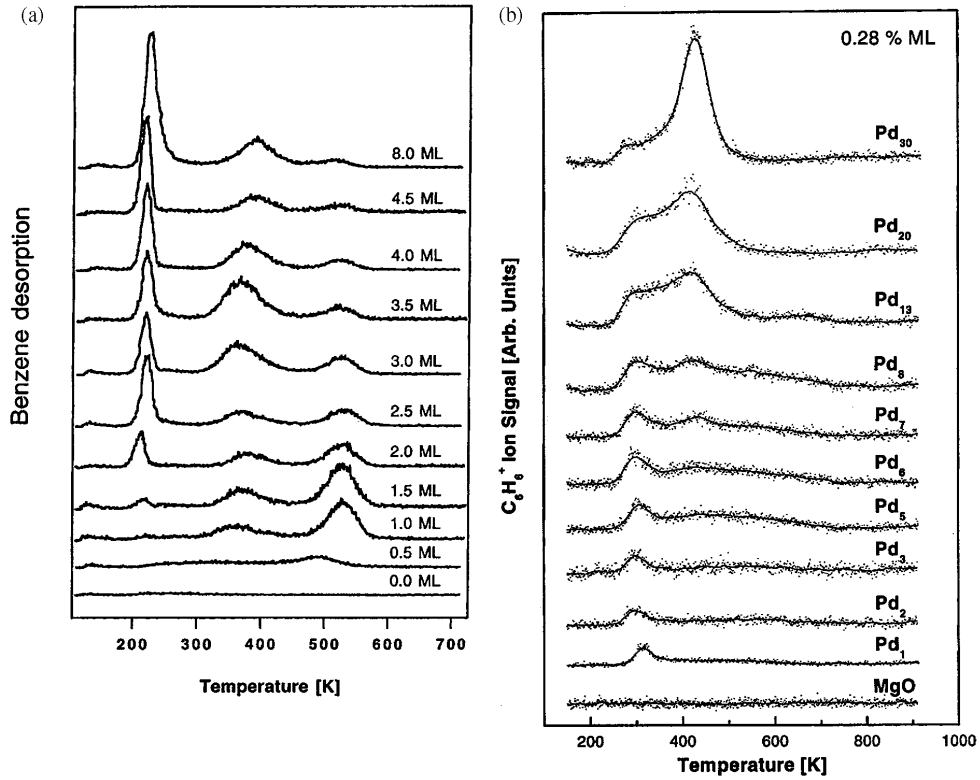


**Figure 21.** (a) Desorption of benzene ($m/e = 78$) following 70 Langmuir acetylene at 150 K for various Pd coverages as indicated and (b) catalytic benzene formation for different Pd cluster sizes obtained from TPR experiments. The bottom spectrum shows that for a clean MgO(100) film no benzene is formed. Cluster coverage is 0.28% for a monolayer for all cluster sizes, where one monolayer corresponds to $2.25 \times 10^{15}$ atoms cm$^{-2}$ ((b) is from [160]).

on Pd and Cu single crystals have shown promising catalytic activity. Structure sensitivity has also been demonstrated [161–163] in high pressure CO + NO reactions over Pd(111) and Pd(100) implying a cluster size effect. In this section the results obtained for CO + NO reaction with respect to cluster size on model Pd and $Cu/Al_2O_3$ catalysts will be discussed. $^{15}NO$ adsorption experiments were carried out on a $Pd/Al_2O_3/Ta(110)$ model catalyst [46] with several different Pd loadings. Clusters were exposed to a background pressure of $1 \times 10^{-7}$ mbar $^{15}NO$ for 5 min at 550 K and then cooled to 350 K prior to $^{15}NO$ removal. The desorption spectra of $^{15}N_2$ and $^{15}N_2O$ over several different Pd loadings are presented in figures 22(a) and (b), respectively. The behaviour is very similar to that found for single crystals. For recombinative $^{15}N_2$ desorption (figure 22(a)), a low temperature feature is observed at $\sim$520 K, along with a high temperature feature above 600 K. The desorption temperature of the low temperature feature is $\sim$70 K higher than on single crystals, consistent with the clusters having an increased concentration of strongly binding step/edge defect sites.

The spectra in figure 22(a) show enhancement of the low temperature $N_a$ (that recombines to $N_2$ or $N_2O$) with increasing cluster size. The peak maximum in each set of spectra shifts to lower temperature with an increase in cluster size. This trend is consistent with smaller clusters with higher surface defect sites stabilizing $N_a$ to a greater extent than the large clusters.

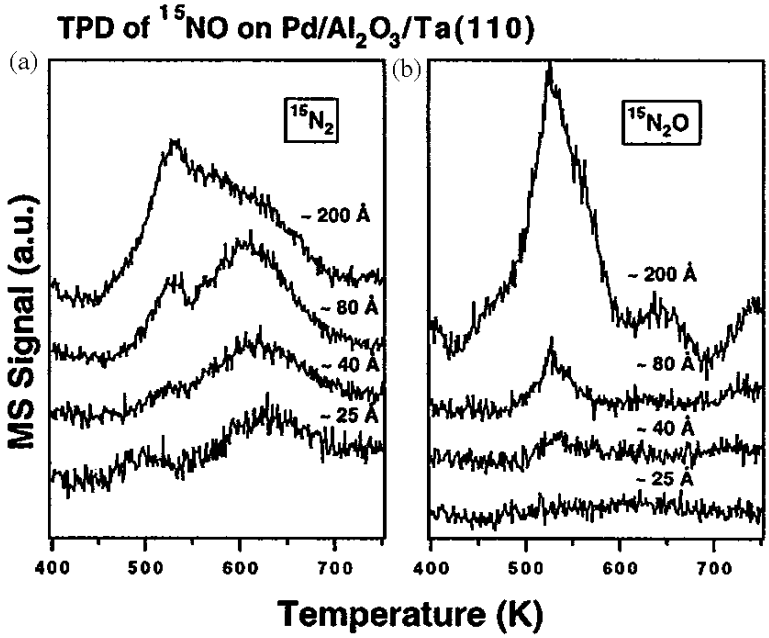


**Figure 22.** TPD monitoring (a) $^{15}N_2$ desorption and (b) $^{15}N_2O$ desorption over several different Pd coverages with the indicated average cluster sizes in a Pd/$Al_2O_3$/Ta(110) catalyst after exposure to $^{15}$NO at 550 K.

Figure 22(b) shows that with an increase in the cluster size, the $N_2O$ desorption feature at ∼530 K appears. Enhancement of the $N_2O$ with increasing cluster size can be understood by comparing the single-crystal data for CO + NO reaction on different faces of Pd. For three different Pd orientations, the $N_2$ selectivity follows the order $\langle 100\rangle \approx \langle 110\rangle > \langle 111\rangle$. This order is consistent with the surface concentration of $N_a$ being enhanced on the more open $\langle 100\rangle$ surface. In other words, the more open surface or the smaller clusters are more reactive towards NO dissociation thereby increasing the concentration of $N_a$ on the surface pushing the $N_2$ selectivity up.

Arrhenius plots are shown in figure 23 for $CO_2$ production from a CO + NO reaction mixture for model oxide-supported Pd, single crystals of Pd and Pd/$Al_2O_3$ powder catalysts. For the powder and model catalysts, a pronounced increase in activity is seen with an increase in cluster size or loading. The larger clusters display the characteristics of the close-packed $\langle 111\rangle$ plane, consistent with the $N_2$ selectivity result.

The reaction of $^{15}$NO with well characterized Cu clusters deposited on highly ordered $Al_2O_3$ films has also been studied using TPD and HREELS [54]. Figure 24 shows that the $^{15}N_2$ formed is sensitive to the cluster size in that no $^{15}N_2$ is detected until $\theta_{Cu} > 0.13$ (∼3.5 nm clusters). Desorption of $^{15}N_2$ was observed at 770 K and was attributed to recombinative desorption from atomic $^{15}N_{(a)}$. The reaction of CO + NO has also been examined for this reactant system. The results show that, in addition to $^{15}N_2$ and $^{15}N_2O$, small amounts of $CO_2$ are produced via reaction between adsorbed CO and atomic oxygen generated from NO dissociation.

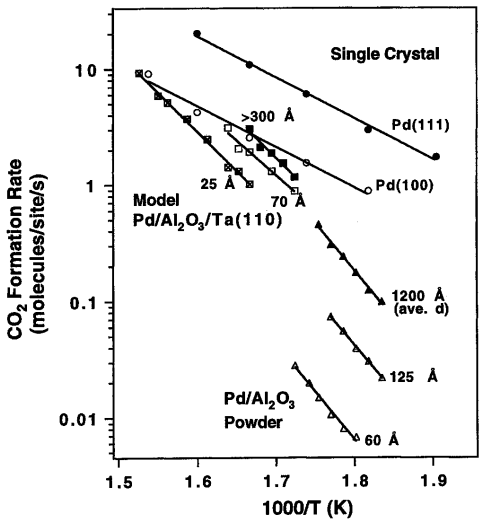


**Figure 23.** Arrhenius plots for CO + NO reaction on single-crystal, model planar supported and $Pd/Al_2O_3$ powder catalysts. The powder catalyst data were taken in the flow reaction mode (4.4:5.2 mbar CO:NO ratio, steady state) and the model catalyst and single-crystal data were acquired for a batch reaction mode in 1 mbar of each reactant.

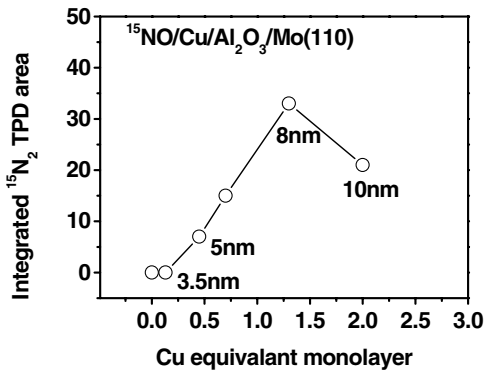


**Figure 24.** The integrated $^{15}N_2$ TPD area ($\beta_2$ state) has been plotted as a function of the Cu coverage (MLE). The average sizes of the Cu clusters are also indicated.

### *5.3. CO oxidation on $Pd/SiO_2$ and $Au/TiO_2$*

Oxidation of CO on transition metals both in the presence and absence of hydrogen in the gas mixture has been of great interest due to its technological importance in the area of automobile exhaust catalyst and in fuel cells [165–175] (in the preferential oxidation step for reducing $CO_x$ level up to few ppm from the hydrogen feed stream). These studies revealed very interesting cluster size effects with respect to the catalytic for certain catalysts. For example, CO oxidation has been studied over $Pd/SiO_2/Mo(100)$ model catalysts [176, 177]. The reaction conditions for the catalysts were 10 mbar CO and 5.0 mbar $O_2$ and reaction temperatures in the range 540–625 K. The conversions were maintained at less than 50% and were monitored using the pressure decrease in a static reactor of known volume (750 $cm^3$). Figure 25 shows Arrhenius plots of CO oxidation over three different model $Pd/SiO_2$ catalysts and a 5% loading of Pd on powdered $SiO_2$. The average cluster sizes were estimated from CO-TPD, $O_2$-TPD and *ex situ*

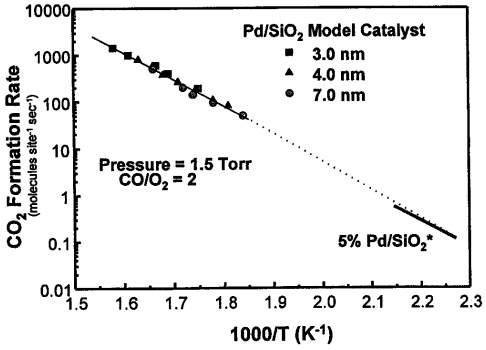


**Figure 25.** Arrhenius plot for CO oxidation with $O_2$ over a model $Pd/SiO_2/Mo(100)$ catalyst and a conventional 5% $Pd/SiO_2$ catalyst. Reaction conditions were $P_{mb} = 0.5$ mbar and $CO/O_2 = 0.2$.

STM/AFM measurements. The specific reaction rates were somewhat higher for the model catalysts than the high surface-area catalysts; however, the activation energies are remarkably similar. This is because in the case of high surface-area catalysts, reaction rates are measured for steady state conditions whereas initial reaction rates are used for model catalysts. These values can differ due to poisoning effects. There was no noticeable dependence of the $CO_2$ formation rate on the Pd cluster size, indicating that CO oxidation over $Pd/SiO_2$ is structure insensitive.

Interestingly, a significant correlation between the cluster size and catalytic activity has been observed for CO oxidation over the $Au/TiO_2$ system [12, 16, 47, 61, 62, 178]. Comparative studies have been carried out on $Au/TiO_2/Mo(100)$ and on $Au/TiO_2(110)$-$(1 \times 1)$. Figures 26(a) and (b) show plots of CO oxidation activity (turnover frequency (TOF) = product molecules/total Au atoms s) at 350 K as a function of Au cluster size supported on $TiO_2(110)$ and $TiO_2/Mo(100)$ substrates. These results show similarities in the structure sensitivity of CO oxidation with a maximum activity evident around the average Au cluster size of $\sim$3 nm on both single-crystal as well as high surface-area [11] $TiO_2$ supports. The observed maximum with respect to cluster size has been related to a metal to nonmetal transition that occurs at cluster size of $\sim$3 nm. Although these catalysts exhibit a high activity for the low temperature CO oxidation, the catalysts are often rapidly deactivated. Using Au(0.25 ML)/$TiO_2/Mo(100)$ as a model system it has been seen that catalysts which exhibit a high initial activity deactivate after a $CO + O_2$ (1:5) reaction of $\sim$120 min at 40 mbar. This deactivation has been attributed to agglomeration of the Au clusters with reaction time and has been documented by detailed STM measurements [12, 16, 47, 61, 62, 178]. The STM data clearly show that under $CO + O_2$ reaction conditions the Au clusters Ostwald ripen; i.e., large clusters grow at the expanse of small ones, depending on the strength of the cluster–support interaction as well as the gas pressure.

### *5.4. Ethane hydrogenolysis*

Extensive studies of ethane hydrogenolysis on various faces of a Ni single crystal have shown that the more open $\langle 100 \rangle$ is significantly more active compared to $\langle 111 \rangle$ [179, 180] and this has been explained as due to geometric [181] and electronic factors [182, 183]. Steric effects arise due to the variation in the Ni–Ni distance while the electronic factor has been associated with the position of the d band leading to different degrees of electron donation into the ethane anti-bonding orbital responsible for C–C bond scission. As expected from the single-crystal results, dramatic particle size effects have been observed on $Ni/SiO_2$ model catalysts (figure 27) [180, 182–184]. The observed maximum in the $CH_4$ formation with respect to the

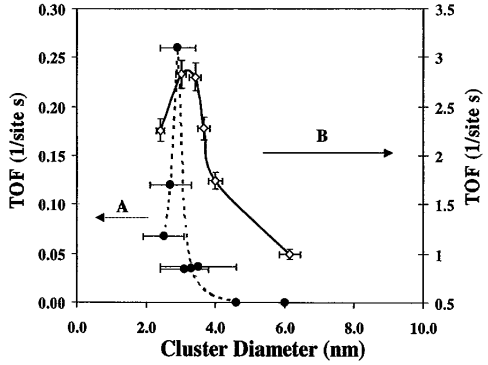


**Figure 26.** CO oxidation TOFs as a function of the Au cluster size supported on $TiO_2$. (A) The $Au/TiO_2$ catalysts were prepared by a precipitation method, and the average cluster size was measured by TEM at 300 K. (B) The $Au/TiO_2$ catalysts were prepared by vapour deposition of Au on planar $TiO_2$ films on Mo(100). The $CO/O_2$ mixture was 1:5 at a total pressure of 40 mbar and 350 K.

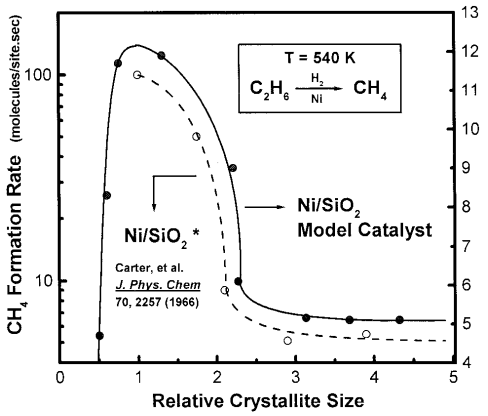


**Figure 27.** $CH_4$ formation rate (molecules/site s) from ethane hydrogenolysis plotted for model and conventional $Ni/SiO_2$ catalysts. Data from [180] are also included for supported Ni catalysts.

initial increase in the average particle size has been understood as due to the increase in the relative nano-facet area ratio $\langle 100\rangle/\langle 111\rangle$ within the particles [93]. Further support has been obtained from the infrared reflection absorption spectroscopy (IRAS) results of CO adsorption on $Ni/SiO_2$ model catalyst as a function of particle size. It has been shown that the total amount of bridge-bonded CO on the Ni clusters parallels the $CH_4$ formation rate with a change in metal cluster size. These results imply that an ensemble effect exists, i.e., only nickel clusters of a particular size possess the necessary chemical properties that lead to maximum activity [93].

## 6. Conclusions and future perspective

It has been shown that it is possible to prepare ultra-thin oxide films with 'bulklike' structural, electronic and chemical properties similar to their bulk analogues. Using such ultra-thin oxide films as a support, model catalysts have been prepared. Indeed the use of thin metal oxide films as supports makes them suitable for ultra-high vacuum measurements, particularly STM and

STS. Changes in the electronic structure as shown by core-level binding energy, band splitting, position of the Fermi level, valence-band dispersion etc with respect to the cluster size have been attributed to both initial and final state effects. More interestingly, a metal to nonmetal transition with respect to the cluster size has been observed by STS and valence band spectra. TEM, TPD and microcalorimetric measurements have provided very useful information regarding the particle morphology and metal support interaction strength. Using *in situ* STM, it has been shown that it is possible to do time-, temperature- and pressure-dependent studies on a cluster-to-cluster basis to provide valuable information regarding cluster growth and sintering kinetics. Size-dependent catalytic reactivity has been observed for a variety of industrially important systems. A critical comparison of acetylene cyclotrimerization on a single crystal of Pd, $Pd/Al_2O_3$ and mass-selected Pd clusters gives some promising clues that will require parallel STM measurements. The CO + NO reaction has been found to be size dependent in terms of selectivity towards $CO_2$, $N_2$ or $N_2O$ production. Finally, low temperature CO oxidation by $O_2$ has been found to have dramatic size dependence for the $Au/TiO_2$ system, the maximum rate occurring at the onset of the metal–nonmetal transition.

## Acknowledgments

We acknowledge with pleasure the support of this work by the Department of Energy, Office of Basic Energy Sciences, and Division of Chemical Sciences and the Robert A Welch Foundation.

## References

[1] Henry C R 1998 *Surf. Sci. Rep.* **31** 235
[2] Baumer M and Freund H J 1999 *Prog. Surf. Sci.* **61** 127
[3] Goodman D W 1995 *Surf. Rev. Lett.* **2** 9
[4] Campbell C T 1997 *Surf. Sci. Rep.* **27** 1
[5] Gunter P L J, Niemantsverdriet J W, Ribeiro F H and Somorjai G A 1997 *Catal. Rev. Sci. Eng.* **39** 77
[6] Diebold U, Pan J M and Madey T E 1995 *Surf. Sci.* **333** 845
[7] Egelhoff W F 1987 *Surf. Sci. Rep.* **6** 253
[8] Freund H J 2002 *Surf. Sci.* **500** 271
[9] Goodman D W 1994 *Surf. Sci.* **300** 837
[10] Goodman D W 1996 *J. Phys. Chem.* **100** 13090
[11] Haruta M 1997 *Catal. Today* **36** 153
Bamwenda G R, Tsubota S, Nakamura T and Haruta M 1997 *Catal. Lett.* **44** 83
[12] Lai X, St Clair T P, Valden M and Goodman D W 1998 *Prog. Surf. Sci.* **59** 25
[13] Mason M G 1983 *Phys. Rev.* B **27** 748
[14] Poppa H 1993 *Catal. Rev. Sci. Eng.* **35** 359
[15] Schneider W D 1993 *Analysis* **21** M20
[16] Valden M, Lai X and Goodman D W 1998 *Science* **281** 1647
[17] Chamber S A 2000 *Surf. Sci. Rep.* **39** 105
[18] Franchy R 2000 *Surf. Sci. Rep.* **38** 195
[19] Muller D A, Sorsch T, Moccio S, Baumann F H, Evans-Lutterodt K and Timp G 1999 *Nature* **399** 758
[20] Ogawa T, Ochiai K, Mochiji K and Hiraiwa A 1991 *Appl. Phys. Lett.* **59** 794
[21] Wertheim G K, Dicenzo S B and Youngquist S E 1983 *Phys. Rev. Lett.* **51** 2310
[22] Wertheim G K 1989 *Z. Phys.* D **12** 319
[23] Dicenzo S B and Wertheim G K 1987 *J. Electron Spectrosc. Relat. Phenom.* **43** C7
[24] Wertheim G K, Dicenzo S B and Buchanan D N E 1986 *Phys. Rev.* B **33** 5384
[25] Wertheim G K 1987 *Phys. Rev.* B **36** 9559
[26] Wertheim G K 1987 *Z. Phys.* B **66** 53
[27] Wertheim G K and Dicenzo S B 1988 *Phys. Rev.* B **37** 844
[28] Wertheim G K 1990 *Phase Transitions* **24** 203
[29] Dicenzo S B and Wertheim G K 1989 *Phys. Rev.* B **39** 6792
[30] Mason M G, Lee S T and Apai G 1980 *Chem. Phys. Lett.* **76** 51

[31] Mason M G, Gerenser L J and Lee S T 1977 *Phys. Rev. Lett.* **39** 288
[32] Mason M G, Lee S T and Apai G 1980 *Chem. Phys. Lett.* **76** 51
[33] Mason M G, Lee S T, Apai G, Davis R F, Shirley D A, Franciosi A and Weaver J H 1981 *Phys. Rev. Lett.* **47** 730
[34] Lee S T, Apai G, Mason M G, Benbow R and Hurych Z 1981 *Phys. Rev.* **23** 505
[35] Apai G, Lee S T and Mason M G 1981 *Solid State Commun.* **37** 213
[36] Cai Y Q, Bradshaw A M, Guo Q and Goodman D W 1998 *Surf. Sci.* **399** L357
[37] Diebold U, Pan J M and Madey T E 1993 *Surf. Sci.* **287** 896
[38] Diebold U, Pan J M and Madey T E 1993 *Phys. Rev.* B **47** 3868
[39] Hovel H, Grimm B, Pollmann M and Reihl B 1998 *Phys. Rev. Lett.* **81** 4608
[40] Hovel H, Grimm B, Pollmann M and Reihl B 1999 *Eur. Phys. J.* D **9** 595
[41] Egelhoff W F and Tibbetts G G 1979 *Phys. Rev.* B **19** 5028
[42] Schneider W D 1994 *Appl. Phys.* A **59** 463
[43] Whetten R L, Cox D M, Trevor D J and Kaldor A 1985 *Phys. Rev. Lett.* **54** 1494
[44] Dicenzo S B, Berry S D and Hartford E H 1988 *Phys. Rev.* B **38** 8465
[45] Rainer D R, Wu M C, Mahon D L and Goodman D W 1996 *J. Vac. Sci. Technol.* A **14** 1184
[46] Rainer D R, Vesecky S M, Koranne M, Oh W S and Goodman D W 1997 *J. Catal.* **167** 234
He J W, Xu X, Corneille J S and Goodman D W 1992 *Surf. Sci.* **279** 119
[47] Valden M, Pak S, Lai X and Goodman D W 1998 *Catal. Lett.* **56** 7
[48] Goodman D W 1996 *J. Vac. Sci. Technol.* A **14** 1526
[49] Guo Q, Oh W S and Goodman D W 1999 *Surf. Sci.* **437** 49
[50] Guo Q, Kim D Y, Street S C and Goodman D W 1999 *J. Vac. Sci. Technol.* A **17** 1887
[51] Guo Q, Lee S and Goodman D W 1999 *Surf. Sci.* **437** 38
[52] Lai X, Chusuei C C, Luo K, Guo Q and Goodman D W 2000 *Chem. Phys. Lett.* **330** 226
[53] Oh W S, Xu C, Kim D Y and Goodman D W 1997 *J. Vac. Sci. Technol.* A **15** 1710
[54] Wu M C and Goodman D W 1994 *J. Phys. Chem.* **98** 9874
[55] Xu X P and Goodman D W 1993 *Surf. Sci.* **282** 323
[56] Luo K, Kim D Y and Goodman D W 2001 *J. Mol. Catal.* A **167** 191
[57] Yang Z, Goodman D W and Wu R 2000 *Phys. Rev.* B **61** 14066
[58] Luo K, St Clair T P, Lai X and Goodman D W 2000 *J. Phys. Chem.* **104** 3050
[59] Liu G, St Clair T P and Goodman D W 1999 *J. Phys. Chem.* **103** 8578
[60] Lai X and Goodman D W 2000 *Prog. Surf. Sci.* **162** 33
Lai X, St Clair T P and Goodman D W 1999 *Faraday Discuss.* **114** 279
[61] Valden M, Lai X and Goodman D W 1998 *Isr. J. Chem.* **38** 285
[62] Lai X and Goodman D W 2000 *J. Mol. Catal.* A **162** 33
[63] Holmblad P M, Rainer D R and Goodman D W 1997 *J. Phys. Chem.* **101** 8883
[64] Xu C, Lai X and Goodman D W 1997 *Phys. Rev.* B **56** 13464
[65] Rainer D R, Xu C, Holmblad P M and Goodman D W 1653 *J. Vac. Sci. Technol.* A **15** 1653
[66] Xu C, Oh W S, Liu G, Kim D Y and Goodman D W 1997 *J. Vac. Sci. Technol.* A **15** 1261
[67] Rainer D R, Korane M, Vesecky S M and Goodman D W 1997 *J. Phys. Chem.* **101** 10769
[68] Rainer D R, Xu C and Goodman D W 1997 *J. Mol. Catal.* A **119** 307
[69] Kolmakov A and Goodman D W 2001 *Surf. Sci.* **490** L597
[70] Kolmakov A and Goodman D W 2000 *Catal. Lett.* **70** 93
[71] Kolmakov A and Goodman D W 2002 *Rev. Sci. Instrum.* submitted
[72] Santra A K, Min B K and Goodman D W 2002 *Surf. Sci.* **515** L475
[73] Santra A K, Min B K and Goodman D W 2002 *J. Vac. Sci. Technol.* A **20** 1897
[74] Haruta M, Tsubota S, Kobayashi T, Ueda A, Sakurai H and Ando M 1993 *Stud. Surf. Sci. Catal.* **75** 2657
[75] Haruta M and Souma Y 1997 *Catal. Today* **36** 1
[76] Haruta M, Uphade B S, Tsubota S and Miyamoto A 1998 *Res. Chem. Int.* **24** 329
[77] Haruta M 1997 *Stud. Surf. Sci. Catal.* **110** 123
[78] Haruta M, Kobayashi T, Sano H and Yamada N 1987 *Chem. Lett.* **2** 405
[79] Haruta M 2001 *Gold. Bull.* **34** 40
[80] Haruta M and Date M 2001 *J. Catal.* **201** 221
[81] He J W, Estrada C A, Corneille J S, Wu M C and Goodman D W 1992 *Surf. Sci.* **261** 164
[82] Wu M C, Corneille J S, Estrada C A, He J W and Goodman D W 1991 *Chem. Phys. Lett.* **182** 472
[83] Wu M C, Estrada C A, Corneille J S and Goodman D W 1992 *J. Chem. Phys.* **96** 3892
[84] He J W, Corneille J S, Estrada C A, Wu M C and Goodman D W 1992 *J. Vac. Sci. Technol.* A **10** 2248, 1467
He J W, Corneille J S, Estrada C A, Wu M C and Goodman D W 1992 *J. Vac. Sci. Technol.* A **10** 1467

[85] Corneille J S, He J W and Goodman D W 1994 *Surf. Sci.* **306** 269
[86] Wu M C, Cornielle J S, He J W, Estrada C S and Goodman D W 1992 *J. Vac. Sci. Technol.* **10** 1467
[87] Kim C M, Yi C W, Min B K, Santra A K and Goodman D W 2002 *Langmuir* **18** 5651
[88] Xu X and Goodman D W 1993 *Surf. Sci.* **282** 323
[89] Xu X, He J W and Goodman D W 1993 *Surf. Sci.* **284** 103
[90] He J W, Xu X, Corneille J S and Goodman D W 1992 *Surf. Sci.* **279** 119
[91] Xu X and Goodman D W 1993 *J. Phys. Chem.* **97** 683
[92] Xu X and Goodman D W 1993 *J. Phys. Chem.* **97** 7711
[93] Coulter K, Xu X and Goodman D W 1994 *J. Phys. Chem.* **98** 1245
[94] Santra A K, Min B K, Kim Y D, Wei T and Goodman D W 2002 *Surf. Sci.* submitted
[95] Chen P J and Goodman D W 1994 *Surf. Sci.* **312** L767
[96] Wu M C and Goodman D W 1994 *J. Phys. Chem.* **98** 9874
[97] Lai X, Chusuei C C, Luo K, Guo Q and Goodman D W 2000 *Chem. Phys. Lett.* **320** 226
[98] Lai X, Guo Q, Min B K and Goodman D W 2001 *Surf. Sci.* **487** 1
[99] Wu Y T, Garfunkel E and Madey T E 1996 *J. Vac. Sci. Technol.* A **14** 2554
[100] Chen P J, Colaianni J S and Yates J T 1990 *Phys. Rev.* B **41** 8025
[101] Crowell J E, Chen J G and Yates J T 1986 *Surf. Sci.* **165** 37
[102] Erskine J L and Strong R L 1982 *Phys. Rev.* B **25** 5547
[103] Strong R L, Firey B, Dewette F W and Erskine J L 1982 *Phys. Rev.* B **26** 3483
[104] Frederick B G, Apai G and Rhodin T N 1990 *J. Electron Spectrosc. Relat. Phenom.* **54** 415
[105] Frederick B G, Apai G and Rhodin T N 1991 *Phys. Rev.* B **44** 1880
[106] Chen J G, Colaianni J S, Weinberg W H and Yates J T 1992 *Surf. Sci.* **279** 223
[107] Chen J G, Crowell J E and Yates J T 1987 *Surf. Sci.* **185** 373
[108] Jaeger R M, Kuhlenbeck H, Freund H J, Wuttig M, Hoffmann W, Frenchy R and Ibach H 1991 *Surf. Sci.* **259** 235
[109] Libuda J, Winkelmann F, Baumer M, Freund H J, Bertrams Th, Neddermeyer H and Muller K 1994 *Surf. Sci.* **318** 61
[110] Bardi U, Atrei A and Rovida G 1992 *Surf. Sci.* **268** 87
[111] Becker C, Kandler J, Raaf H, Linke R, Pelster T, Drager M, Tanemura M and Wandelt K 1998 *J. Vac. Sci. Technol.* A **16** 1000
[112] Rosenhahn A, Schneider J, Becker C and Wandelt K 1999 *Appl. Surf. Sci.* **142** 169
[113] Schroeder T, Adelt M, Richter B, Naschitzki M, Baumer M and Freund H J 2000 *Surf. Rev. Lett.* **7** 7
[114] Santra A K, Min B K and Goodman D W 2002 *Surf. Sci.* submitted
[115] Kundu M and Murata Y 2002 *Appl. Phys. Lett.* **80** 1921
[116] Wang J, Mitchell C E J, Egdell R G and Foord J S 2002 *Surf. Sci.* **506** 66
[117] Engel T 1993 *Surf. Sci. Rep.* **18** 91
[118] Hattori T 1995 *Crit. Rev. Solid State Mater. Sci.* **20** 339
[119] Wollschlager J, Erdos D and Schroder K M 1998 *Surf. Sci.* **404** 272
[120] Gallagher M C, Fyfield M S, Cowin J P and Joyce S A 1995 *Surf. Sci.* **339** L909
[121] Schintke S, Messerli S, Pivetta M, Patthey F, Libio L, Stengel M, De Vita A and Schneider W D 2001 *Phys. Rev. Lett.* **87** 276801
[122] Park Y, Fullerton E E and Bader S D 1995 *J. Vac. Sci. Technol.* A **13** 301
[123] Kolmakov A and Goodman D W 2002 *Chem. Res.* at press
[124] Chusuei C C, Lai X, Luo K and Goodman D W 2001 *Top. Catal.* **14** 71
[125] Hensen K H, Worren T, Stempel S, Laegsgaard E, Baumer M, Freund H J, Besenbacher F and Stensgaard I 1999 *Phys. Rev. Lett.* **83** 4120
[126] Morgenstern K, Rosenfeld G, Laegsgaard E, Besenbacher F and Cosma G 1998 *Phys. Rev. Lett.* **80** 556
[127] Hensen K H, Worren T, Laegsgaard E, Besenbacher F and Stensgaard I 2001 *Surf. Sci.* **475** 96
[128] Worren T, Hensen K H, Laegsgaard E, Besenbacher F and Stensgaard I 2001 *Surf. Sci.* **477** 8
[129] Santra A K, Min B K and Goodman D W 2002 *Surf. Sci.* **513** L441
[130] Clark P G and Friend C M 1999 *J. Chem. Phys.* **111** 6991
[131] Bennett R A, Pang C L, Perkins N, Smith R D, Morrall P, Kvon R I and Bowker M 2002 *J. Phys. Chem.* **106** 4688
Bowker M, Stone P, Bennett R and Perkins N 2002 *Surf. Sci.* **497** 155
[132] Bowker M, Smith R D and Bennett R A 2001 *Surf. Sci.* **478** L309
[133] Bennett R A, Stone P and Bowker M 1999 *Catal. Lett.* **59** 99
[134] Bennett R A, Stone P, Price N J and Bowker M 1999 *Phys. Rev. Lett.* **82** 3831
[135] Stone P, Poulston S, Bennett R A and Bowker M 1998 *Chem. Commun.* 1369

[136] Mitchell C E J, Howard A, Carney M and Egdell R G 2001 *Surf. Sci.* **490** 196
[137] Howard A, Mitchell C E J and Egdell R G 2002 *Surf. Sci.* **515** L504
[138] Yang X J and Perry S S 2002 *Surf. Sci.* **506** L261
[139] Santra A K and Goodman D W in preparation
[140] First P N, Stroscio J A, Dragoset R A, Pierce D T and Celotta R J 1989 *Phys. Rev. Lett.* **63** 1416
[141] Poppa H 1967 *J. Appl. Phys.* **38** 3883
[142] Heinemann K, Osaka T, Poppa H and Avalos-Borja M 1983 *J. Catal.* **83** 61
[143] Heinemann K, Osaka T and Poppa H 1983 *Ultramicroscopy* **12** 9
[144] Goyhenex C and Henry C R 1994 *Phil. Mag.* A **69** 1073
[145] Nepijko S A, Klimenkov M, Kuhlenbeck H, Zemlyanov D, Herein D, Schlogl R and Freund H J 1998 *Surf. Sci.* **412/413** 192
[146] Klimenkov M, Nepijko S, Kuhlenbeck H, Baumer M, Schlogl R and Freund H J 1997 *Surf. Sci.* **391** 27
[147] Starr D E, Bald D J, Musgrove J E, Ranney J T and Campbell C T 2001 *J. Chem. Phys.* **114** 3752
[148] Campbell C T, Grant A W, Starr D E, Parker S C and Bondzie V A 2001 *Top. Catal.* **14** 43
Parker S C, Grant A W, Bondzie V A and Campbell C T 1999 *Surf. Sci.* **441** 10
[149] Starr D E and Campbell C T 2001 *J. Phys. Chem.* **105** 3776
[150] Larsen H, Starr D E and Campbell C T 2001 *J. Chem. Thermodyn.* **33** 333
[151] Ormerod R M, Lambert R M, Hoffmann H, Zaera F, Yao J M, Saldin D K, Wang L P, Bennett D W and Tysoe W T 1993 *Surf. Sci.* **295** 277
[152] Ormerod R M, Lambert R M, Hoffmann H, Zaera F, Wang L P, Bennett D W and Tysoe W T 1994 *J. Phys. Chem.* **98** 2134
[153] Ormerod R M, Lambert R M, Hoffmann H, Bennett D W and Tysoe W T 1995 *Surf. Sci.* **330** 1
[154] Tysoe W T, Nyberg G L and Lambert R M 1983 *Surf. Sci.* **135** 128
[155] Tysoe W T, Nyberg G L and Lambert R M 1983 *Chem. Commun.* 623
[156] Tysoe W T, Nyberg G L and Lambert R M 1983 *J. Phys. Chem.* **90** 3188
[157] Tysoe W T, Ormarod R M, Lambert R M, Zgrablich G and Ramirezcuesta A 1993 *J. Phys. Chem.* **97** 3365
[158] Tysoe W T 1998 *Isr. J. Chem.* **38** 313
[159] Yoshinobu J, Sekitani T, Onchi M and Nishijima M 1990 *J. Phys. Chem.* **94** 4269
[160] Abbet S, Sanchez A, Heiz U, Schneider W D, Ferrari A M, Pacchioni G and Rosch N 2000 *Surf. Sci.* **454** 984
[161] Vesecky S M, Rainer D R and Goodman D W 1996 *J. Vac. Sci. Technol.* A **14** 1457
[162] Vesecky S M, Chen P J, Xu X P and Goodman D W 1995 *J. Vac. Sci. Technol.* A **13** 1539
[163] Xu X P, Chen P J and Goodman D W 1994 *J. Phys. Chem.* **98** 9242
[164] Fink T, Dath J P, Imbihl R and Ertl G 1991 *Surf. Sci.* **251** 985
[165] Szanyi J and Goodman D W 1994 *J. Phys. Chem.* **98** 2972
[166] Szanyi J, Kuhn W K and Goodman D W 1994 *J. Phys. Chem.* **98** 2978
[167] Goodman D W, Peden C H F, Fisher G B and Oh S H 1993 *Catal. Lett.* **22** 271
[168] Szanyi J and Goodman D W 1993 *Catal. Lett.* **21** 165
[169] Peden C H F, Goodman D W, Weisel M D and Hoffmann F M 1991 *Surf. Sci.* **253** 44
[170] Berlowitz P J, Peden C H F and Goodman D W 1988 *J. Phys. Chem.* **92** 5213
[171] Peden C H F, Goodman D W, Blair D S, Berlowitz P J, Fisher G B and Oh S H 1988 *J. Phys. Chem.* **92** 1563
[172] Goodman D W and Peden C H F 1986 *J. Phys. Chem.* **90** 4839
[173] Peden C H F and Goodman D W 1985 *J. Vac. Sci. Technol.* **3** 1558
[174] Eiswirth M, Moller P, Wetzl K, Imbihl R and Ertl G 1989 *J. Chem. Phys.* **90** 510
Imbihl R, Ladas S and Ertl G 1988 *J. Vac. Sci. Technol.* A **6** 877
[175] Santra A K and Goodman D W 2002 *Electrochim. Acta* **47** 3595
[176] Rainer D R, Koranne M, Vesecky S M and Goodman D W 1997 *J. Phys. Chem.* B **101** 10769
[177] Rainer D R, Wu M C, Mahon D L and Goodman D W 1996 *J. Vac. Sci. Technol.* A **14** 1184
[178] Iizuka Y, Fujiki H, Yamauchi N, Chijiiwa T, Arai S, Tsubota S and Haruta M 1997 *Catal. Today* **36** 115
[179] Goodman D W 1982 *Surf. Sci.* **123** L679
[180] Carter J L, Cusumano J A and Sinfelt J H 1966 *J. Phys. Chem.* **70** 2257
[181] Desjonqueres M C and Cyrot-Lackmann F 1976 *J. Chem. Phys.* **64** 3707
[182] Kiskinova M and Goodman D W 1981 *Surf. Sci.* **108** 64
[183] Goodman D W 1992 *Catal. Today* **12** 189
[184] Martin G A 1979 *J. Catal.* **60** 452